nature electronics

Supplementary information

https://doi.org/10.1038/s41928-025-01357-7

A high-frequency artificial nerve based on homogeneously integrated organic electrochemical transistors

In the format provided by the authors and unedited

This PDF file includes:

Supplementary Tables 1-5

Supplementary Figures 1-39

References

Table of contents

Table S1 | Summary of the state-of-the-art artificial nerves.

Refs.	Sensing modality	Processing function	Memory	Bio-compatibility	Mechanical Flexibility	Animal test	Voltage supply	Elements for integration
[1]	Pressure	Frequency encoding	Short-term	Not verified	Yes	Yes	~4.6 V (depends on the oscillator)	Heterogeneous (CNT sensor+ Organic Oscillator+ Organic transistor)
[2]	Pressure	No	Short-term	Not verified	Yes	Yes	~5 V (depends on the CMOS I/V converter	Heterogeneous (CNT sensor+ Organic transistor + CMOS I/V converter)
[3]	Chemical and Optical signal	Frequency encoding	Long/ short-term	Not verified	No	No	~5 V (depends on the CMOS sensor)	Heterogeneous (CMOS sensor + Inorganic memristor + Organic hydrogel)
[4]	Chemical signals	No	Long-term	Verified by cell culture	Yes	Yes	~1.5 V (depends on the inorganic memristor)	Heterogeneous (CNT/GO sensor + Inorganic memristor + Organic hydrogel)
This work	Chemical, optical, and electrical signals	Frequency encoding, amplify, threshold.	Long/ short-term	Verified by cell culture and animal implantation	Yes	Yes	1 V	Homogeneous (All-OECTs)

Table S2 | Comparison of the state-of-the-art OECTs with the blended channel.

		Vertical IGTs	Vertical OECTs with Cin-Cell	Sv-OECTs with GIBS
Refs.		[5,6]	[7,8]	This work
Device concept	Materials	Directly blend the hydrophilic materials with OMIECs to confine the ions within the channel and accelerate the ion transport	Directly blend the Cin-Cell with OMIECs to stabilize the device and accelerate the ion transport and	Sequential deposit the biocompatible and hydrophilic dopant onto OMIECs.
	Microstructure control	As-cast	As-cast	Gradient-intermixed bicontinuous structure (GIBS)
	Effect	Can only improve the ion transport; the charge transport and ion storage can be worse because of the intermixing of isolating materials.	Can only improve ion transport and device stability. No demonstration of charge transport or ion storage improvement.	Improve both ion and charge transport by doping and forming continuous and ordered ion and charge transport pathways
Performance		Only improve the τ (900 ns for $W*d$=5*0.1 μm^2 device)	Only improve the τ (65 μs for $W*d$=5*5 μm^2 device, ref 12) (366 μs for $W*d$=30*30 μm^2 device, ref 11)	Improve both g_m and τ (recorded-low value of 27 μs for $W*d$=50*50 μm^2 device)
Functions	Volatile Sensing	Only electrical signals; cannot sense the chemical species because of the lack of external electrolyte	At least chemical and electrical signals	Chemical, optical, electrical signals…
	Non-volatile Memory	Not verified (hard to realize because the ions can only stay within the swelled channel, which lacks the trapping site of ions)	Not verified	Yes (>100 kHz write-read operation and >1,000 s retention)
	Biocompatibility	Claimed but not verified	Not verified	Yes
Universality		Not verified	Yes	Yes
Evolvability for ANs		Not verified (hard to realize because of the lack of memory function)	Not verified (hard to realize because of the lack of memory function)	Yes

Table S3 | Summary of state-of-the-art *n*-type EGTs.

Materials	Electrolyte	V_{th} (V)	τ (s)	g_m (mS)	g_m/τ (mS/S)	W (μm)	d (μm)	L (μm)	$\tau/[(WL)^{1/2} d]$ (s/μm^2)	Ref.	Classification
ZnO	EMIMTFSI: SEAS-N_3	-0.5	-	2.5	-	200	0.05	10	-	9	
MoS_2	EMIMTFSI Ion-gel	0.2	0.7	0.6	0.86	~20	~0.0012	~2	92.2	10	Non-organic EGTs
IGZO	Cellulose hydrogel	0.25	0.085	3.9	458.82	6800	0.035	40	4.65E-3	11	
Graphene	PBS	0.44	-	0.25	-	-	-	20	-	12	
BBL	0.1 M NaCl	0.21	0.900	9.7	10.8	39000	0.18	20	5.66E-3	13	
BBL:PEI	0.1 M NaCl	-0.45	0.167	0.28	1.68	1000	0.05	30	1.93E-2	14	
BBL: MWCNTs	0.1 M NaCl	0.2	0.024	0.032	1.33	1000	0.04	30	3.46E-3	15	
p(gNDI-gT2)	0.1 M NaCl	0.28	0.005	0.022	4.34	100	0.35	10	4.52E-4	16	
P90	0.1 M NaCl	0.24	0.041	0.001	0.02	100	0.087	10	1.49E-2	17	
P90:TBAF	0.1 M NaCl	0.22	0.024	0.011	0.44	100	0.116	10	6.54E-3	18	
PgNAN	0.1 M NaCl	0.37	0.127	0.212	1.67	100	1.5	10	2.68E-3	19	
f-BTI2TEG-FT	0.1 M NaCl	0.45	0.272	2.4	8.82	5000	0.021	5	8.2E-2	20	
f-BTI2g-TVTCN	0.1 M NaCl	0.68	0.052	0.8	15.38	100	0.042	10	3.92E-2	21	
f-BseI2g-SVSCN	0.1 M NaCl	0.68	5.1E-3	1.4	274.5	100	23	10	7.01E-3	22	
BBL_{152}	0.1 M NaCl	0.15	3.80E-4	0.044	115.79	20	0.02	10	1.34E-3	23	
PBFDO	0.1 M NaCl	-0.23	0.100	11.2	112.00	-	0.055	-	-	24	Polymer EGTs
P(gTDPP2FT)	0.1 M NaCl	0.56	1.75E-3	0.9	514.29	100	0.06	10	9.22E-4	25	
BBL	0.1 M NaCl	0.19	5.2E-3	0.065	12.5	100	0.08	10	2.06E-3	17	
p(C2F-V)	0.1 M NaCl	0.02	3.36E-4	2.25	6696.4	100	0.09	10	1.18E-4	26	
Homo-gDPP (Vertical)	0.1 M NaCl	0.33	3.66E-4	59.5	162568	30	30	0.1	9.96E-6	7	
Homo-gDPP (Planar)	0.1 M NaCl	0.55	2.69E-4	0.48	1784.4	100	0.1	10	8.51E-5	7	
bHOMO-gDPP (Vertical)	0.1 M NaCl	-	6.5E-5	~25	384615	5	5	0.1	2.60E-5	7	
	0.1 M NaCl	0.45	1.54E-4	~45	292208	10	10	0.1	2.18E-5	7	
	0.1 M NaCl	-	3.15E-4	~120	380952	30	30	0.1	8.57E-6	7	
	0.1 M NaCl	-	3.88E-4	~180	463918	50	50	0.1	4.91E-6	7	
	0.1 M NaCl	-	4.51E-4	~350	776053	100	100	0.1	2.02E-6	7	
	0.1 M NaCl	-	4.79E-4	~700	1461378	200	200	0.1	7.57E-7	7	
C_{60}TEG	0.1 M KCl	0.55	0.080	0.004	0.051	400	0.14	20	6.38E-3	27	Small molecule

TDPP-RD-G7	0.1 M NaCl	0.34	0.0105	3.5	333.33	34000	0.01	20	1.27E-3	[28]	EGTs
BBL *W*=*d*=50 um	0.1 M NaCl	0.3	0.04722	5.2	110.12	50	50	0.021	4.61E-4	-	
BBL/PEI (GIBS) *W*=*d*=50 um	0.1 M NaCl	-0.1	2.7E-5	13.7	507407	50	50	0.023	7.12E-7	-	Polymer EGTs (This work)
BBL/PEI (GIBS) *W*=*d*=300 um	0.1 M NaCl	-0.13	1.85E-4	96	518918	300	300	0.023	3.32E-7	-	

We note the response time of EGTs is related to the ion/charge transport resistance and capacitance of the device. Thus, it has the following expression:

$$\tau \propto RC \qquad (1)$$

Where *R* and *C* denotes ion/charge transport resistance and channel capacitance of OECTs. *R* can be further written as [29]:

$$R=\rho(WL)^{-1/2} \qquad (2)$$

Thus, equation (1) can be further written as:

$$\tau=RC= \rho(WL)^{-1/2}\, C^*WLd= (C^*\rho)\,(WL)^{1/2}d \qquad (3)$$

In this equation, $C^*\rho$ *is* the intrinsic character of channel materials, which directly reflects the ion/charge transport behavior of materials. $C^*\rho$ can be evaluated by:

$$C^*\rho=\tau/[(WL)^{1/2}d] \qquad (4)$$

To compare this character, we calculated and summarized the $\tau/(WL)^{1/2}d$ value in Table S3. The BBL/PEI-based device shows the lowest $\tau/(WL)^{1/2}d$, indicating the highest ion/charge transport capability of the sv-OECT channel with the GIBS. Specially, for vertical EGTs, as the ions can be injected from both sides of the channel, this equation should be written as:

$$C^*\rho=\tau/[(2WL)^{1/2}(d/2)] \qquad (5)$$

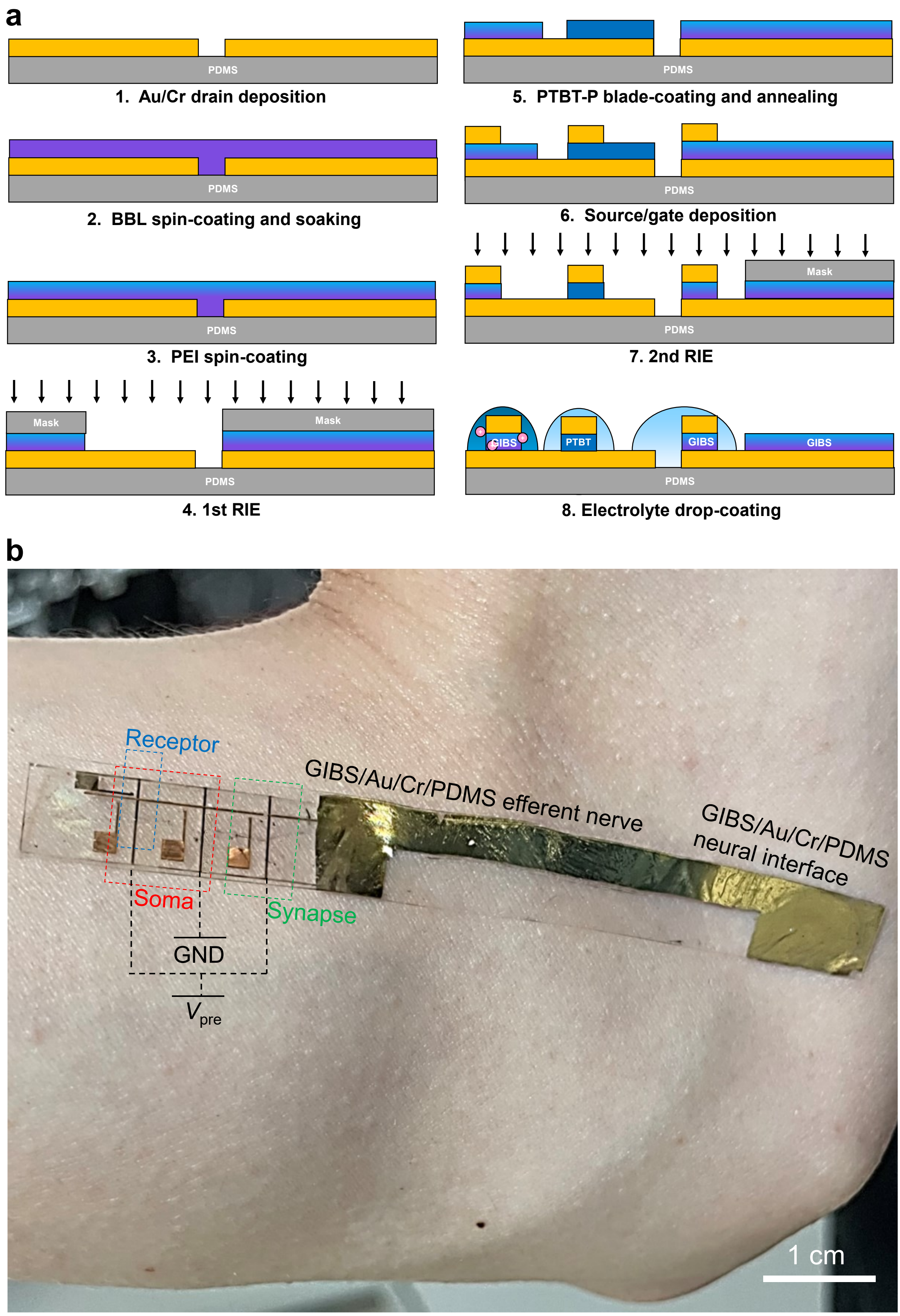

Fig. S1 | Schematics of flexible CMAN fabrication and circuit diagram.

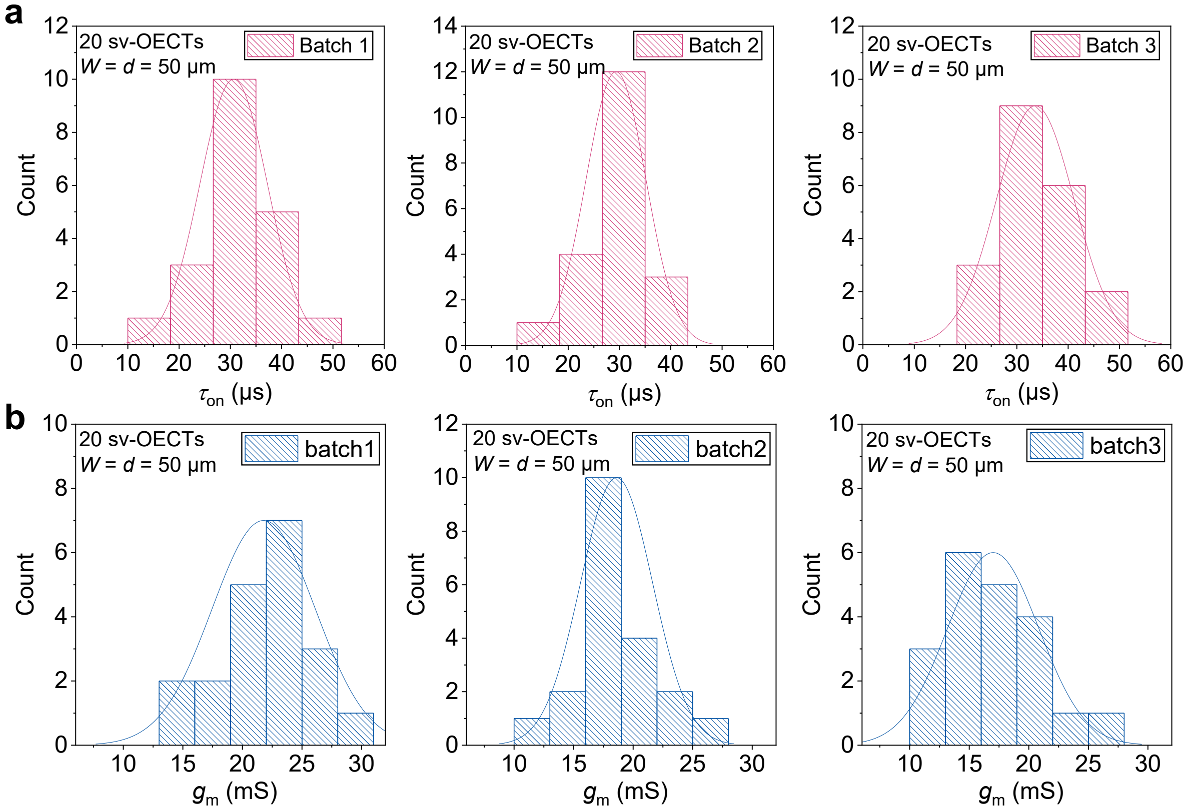

Fig. S2 | Reproducibility of sv-OECT. a, Reproducibility of sv-OECT response speed (τ_{on}). b, Reproducibility of sv-OECT transconductance (g_m). $W = d = 50$ μm, $L = 25$ nm, W, d, L denote the width, thickness and length of channel, d_{PEI}/d_{BBL}=0.5, data from $n = 60$ devices, 3 batches.

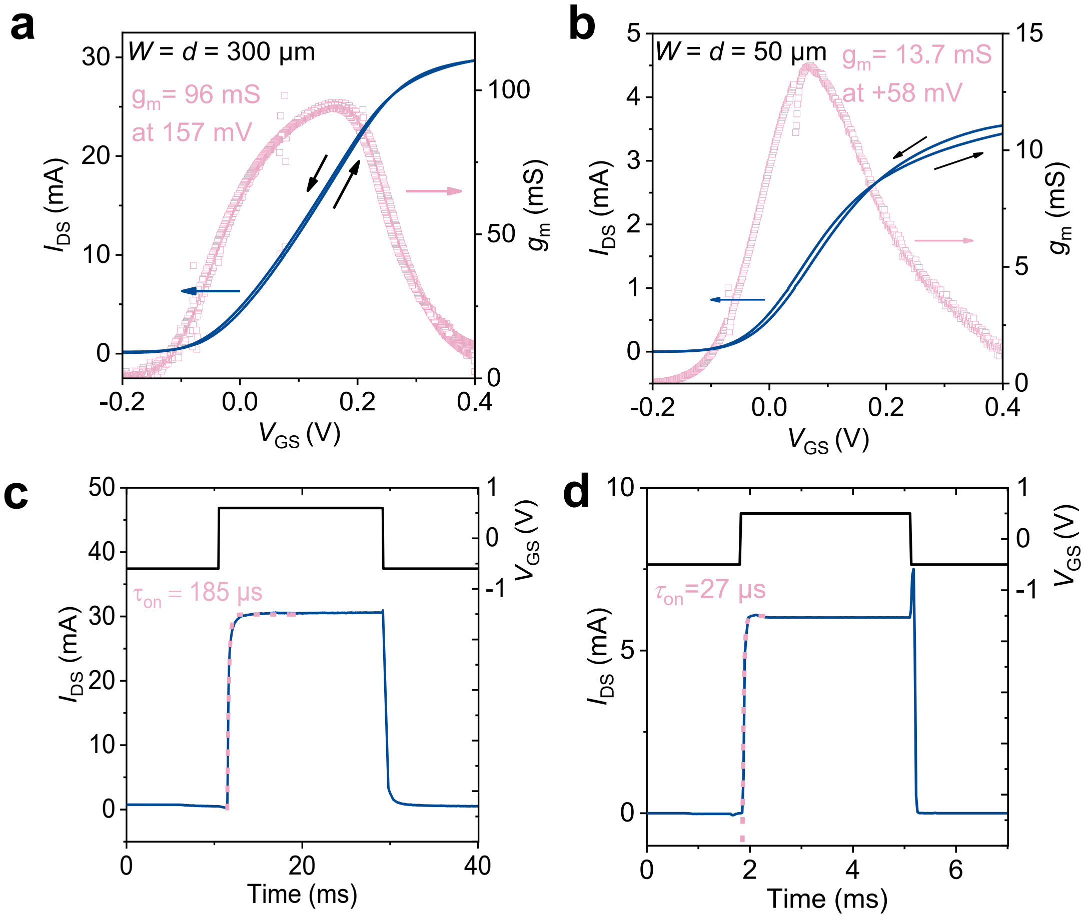

Fig. S3 | Performances of sv-OECTs with different channel dimension. a-b, Transfer curves of a, sv-OECT with $W = d = 300$ µm, $L = 23$ nm, and b, sv-OECT with $W = d = 50$ µm, $L = 23$ nm. c-d, Transient response of c, sv-OECT with $W = d = 300$ µm, $L = 23$ nm, and d, sv-OECT with $W = d = 50$ µm, $L = 23$ nm. Drain voltage, $V_{DS} = 0.4$ V, I_{DS} and V_{GS} denote the channel current and gate voltage, black arrows denote the scanning direction. For all the tests, $d_{PEI}/d_{BBL} = 0.5$.

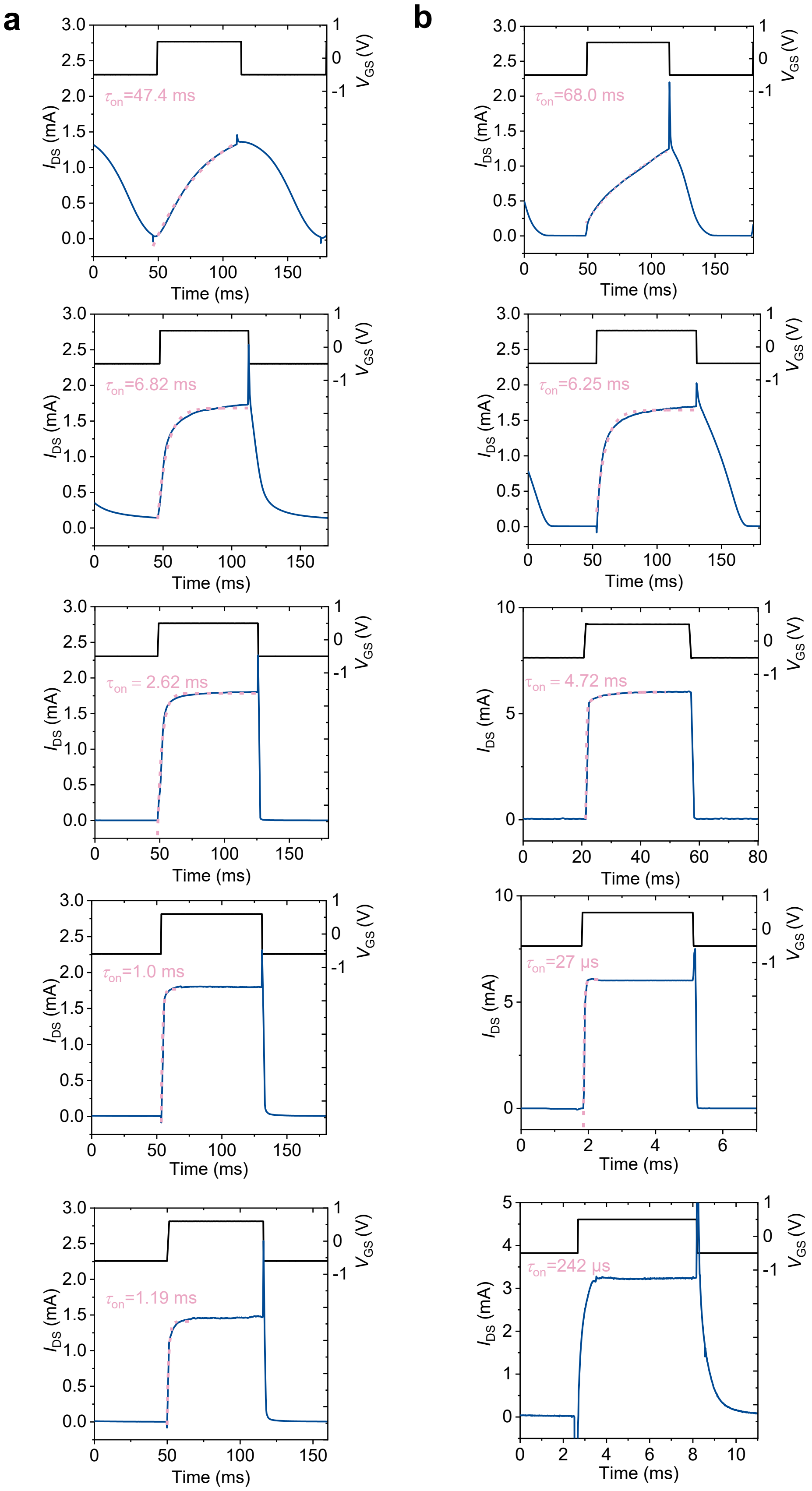

Fig. S4 | Temporal response of the drain current of sv-OECTs with different PEI to BBL ratios. a, As cast devices and b, Thermal annealed devices. From top to bottom: d_{PEI}/d_{BBL}=0, 0.05, 0.25, 0.5, 1.0. For all the tests, $W = d = 50$ μm.

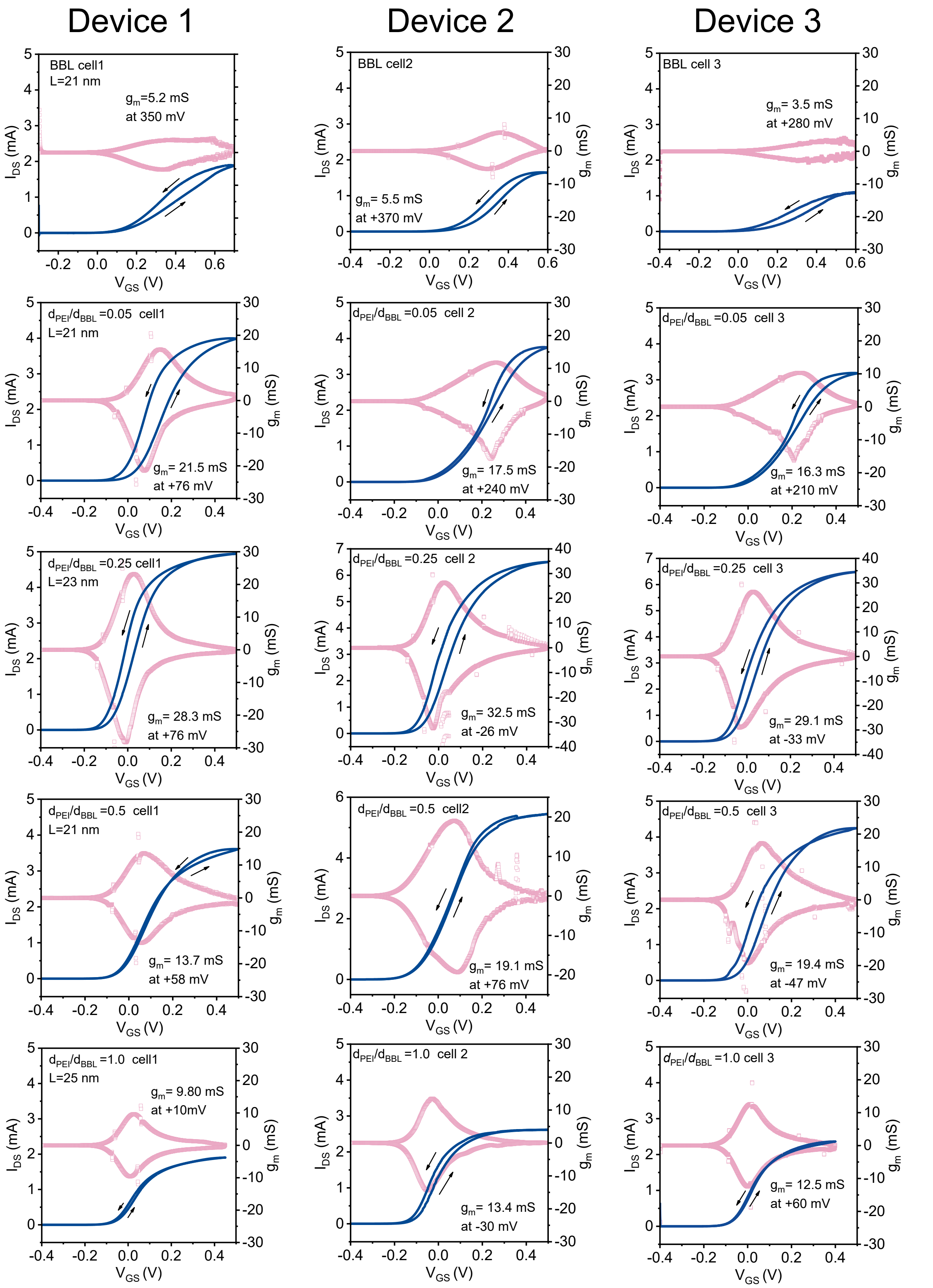

Fig. S5 | Transfer curves of sv-OECTs with different PEI to BBL ratio. From top to bottom: $d_{\mathrm{PEI}}/d_{\mathrm{BBL}}$=0, 0.01, 0.05, 0.10, 0.20. Transfer curves (blue lines) were measured at 55 mV/s. Transconductance (g_m) curves were extracted using the the following equation: $g_m = \partial I_{\mathrm{DS}}/\partial V_{\mathrm{GS}}$. For all the tests, $W = d = 50$ μm.

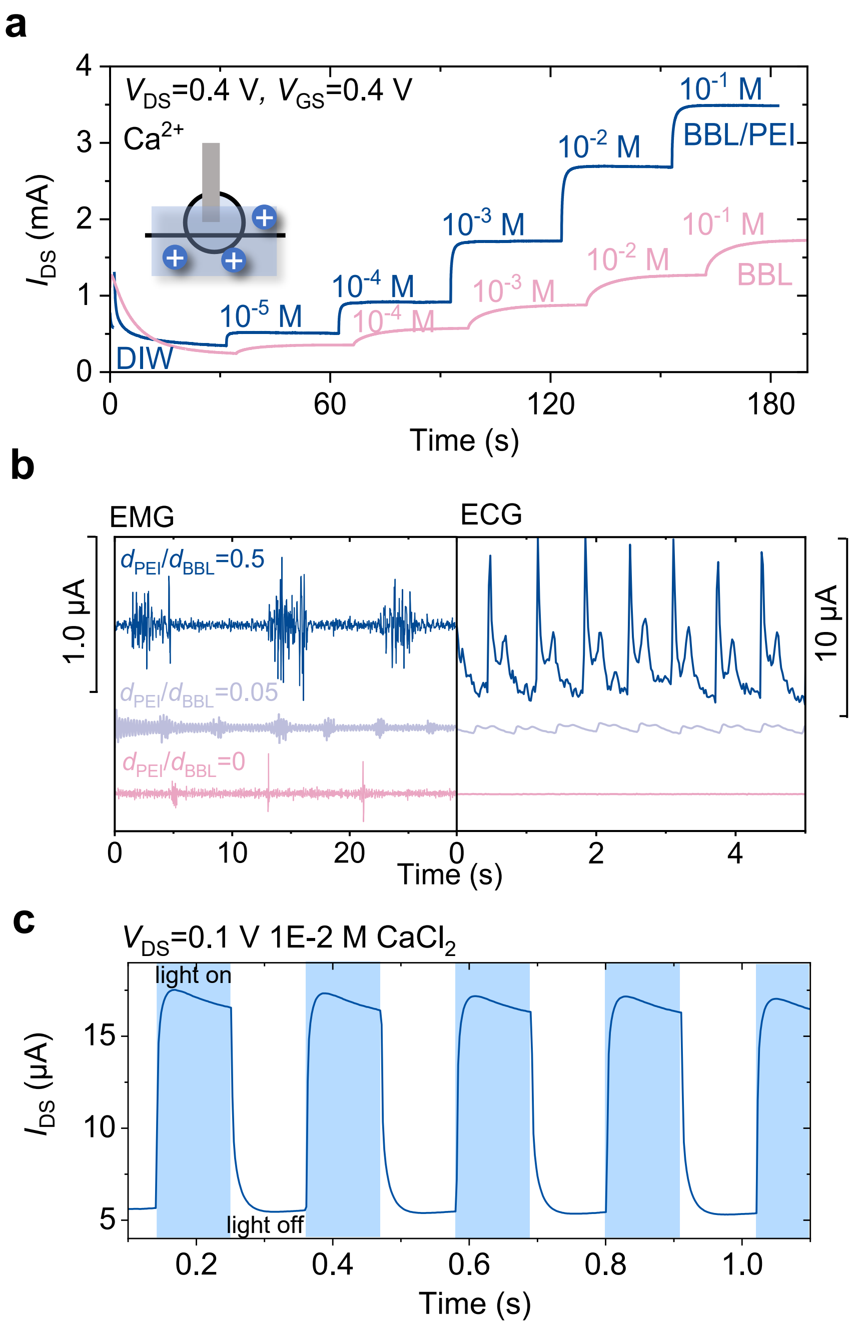

Fig. S6 | sv-OECT acts as a multimodal receptor. a, Transient I_{DS} response of *n*-type sv-OECT receptors as a function of time as successive amounts of Ca^{2+} were added. b, The human electrocardiogram (ECG) and electromyogram (EMG) signals recorded by the sv-OECT receptor, from up to bottom: d_{PEI}/d_{BBL} = 0.5, 0.05, 0. ECG and EMG signas were collected from a healthy male volunteer aged 28. Two medical gel-assisted Ag/AgCl ECG electrodes were pasted on to the skin over the left and right chest, and then connected to the gate and grounded source of the sv-OECT using two teflon shielded cables, respectively. Signal was recorded by monitoring the I_{DS} using one channel of Keithley 2602B SMU. c, Transient I_{DS} response of sv-OECT receptor upon light stimuli (455 nm, 100 mW/cm^2, V_{DS}=0.1 V, blue shadings indicate the light on stage).

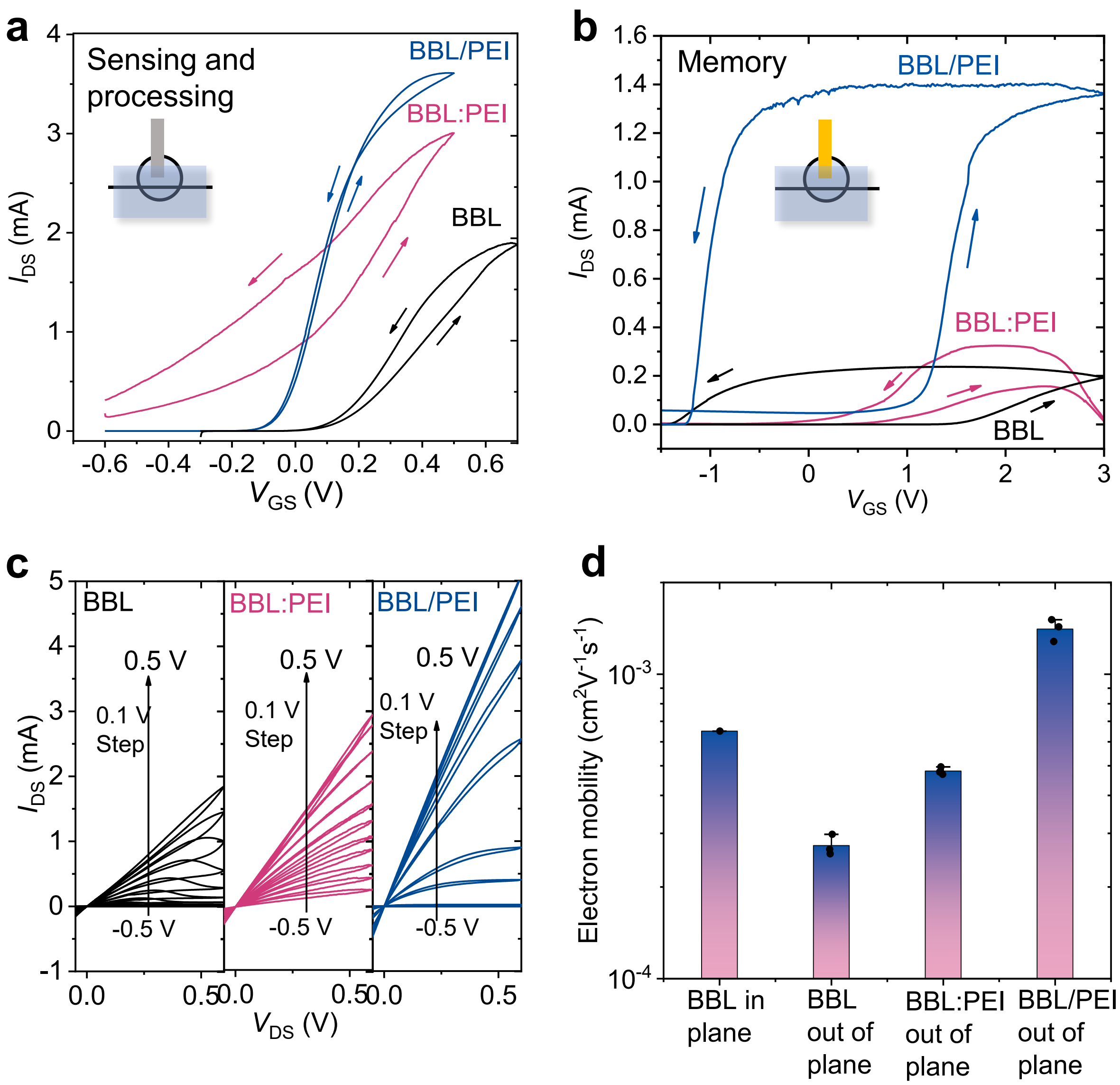

Fig. S7 | Comparison of BBL, BBL/PEI and BBL:PEI based v-OECTs. a, Transfer curves measured at 55 mV/s (gated by Ag/AgCl and 0.1 M NaCl aqueaous solution). b, Transfer curves measured at 0.5 V/s (gated by Au and EMIMTFSI ion gel). c, Output curves measured at 70 mV/s (gated by Ag/AgCl and 0.1 M NaCl aqueous solution). d, Electron mobility measured by space charge limited current (SCLC) method. Error bars denote the s.d. for $n = 3$ independent devices, mean ± s.d.. The in-plane mobility is extracted from reference [30]. For all the tests, $W = d = 50$ μm, $d_{PEI}/d_{BBL} = 0.5$.

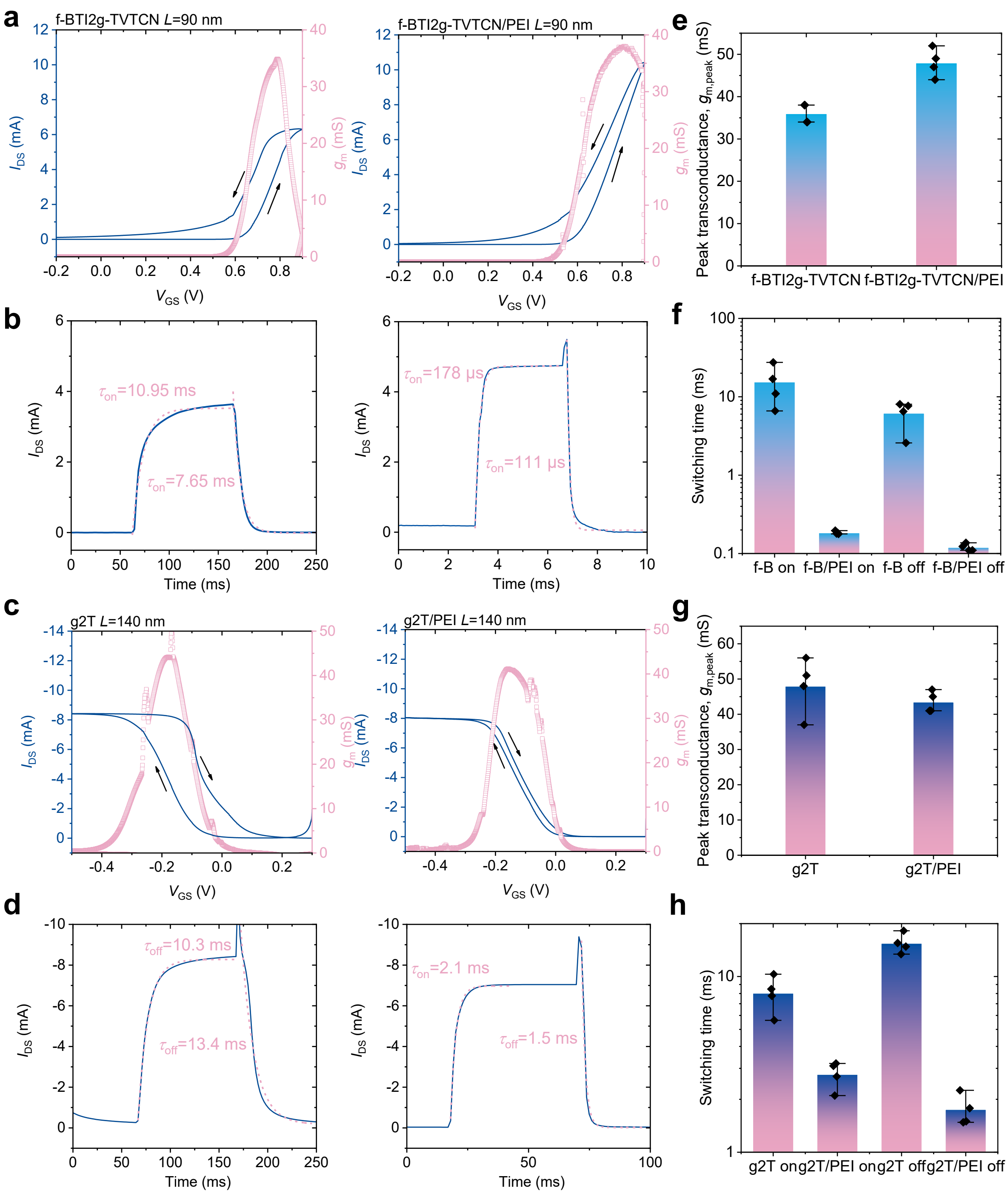

Fig. S8 | Universality of GIBS strategy. a-b, Transfer curves and transient response of f-BTI2g-TVTCN v-OECT and f-BTI2g-TVTCN/PEI sv-OECTs. c-d, Transfer curves and transient response of g2T v-OECT and g2T/PEI sv-OECT. e-h, Volatile switching time and peak transconductance comparison of the v-OECTs and sv-OECTs ($W = d = 50$ μm, $L \sim 25$ nm, error bars denote the s.d. for $n = 4$ independent devices, mean ± s.d.).

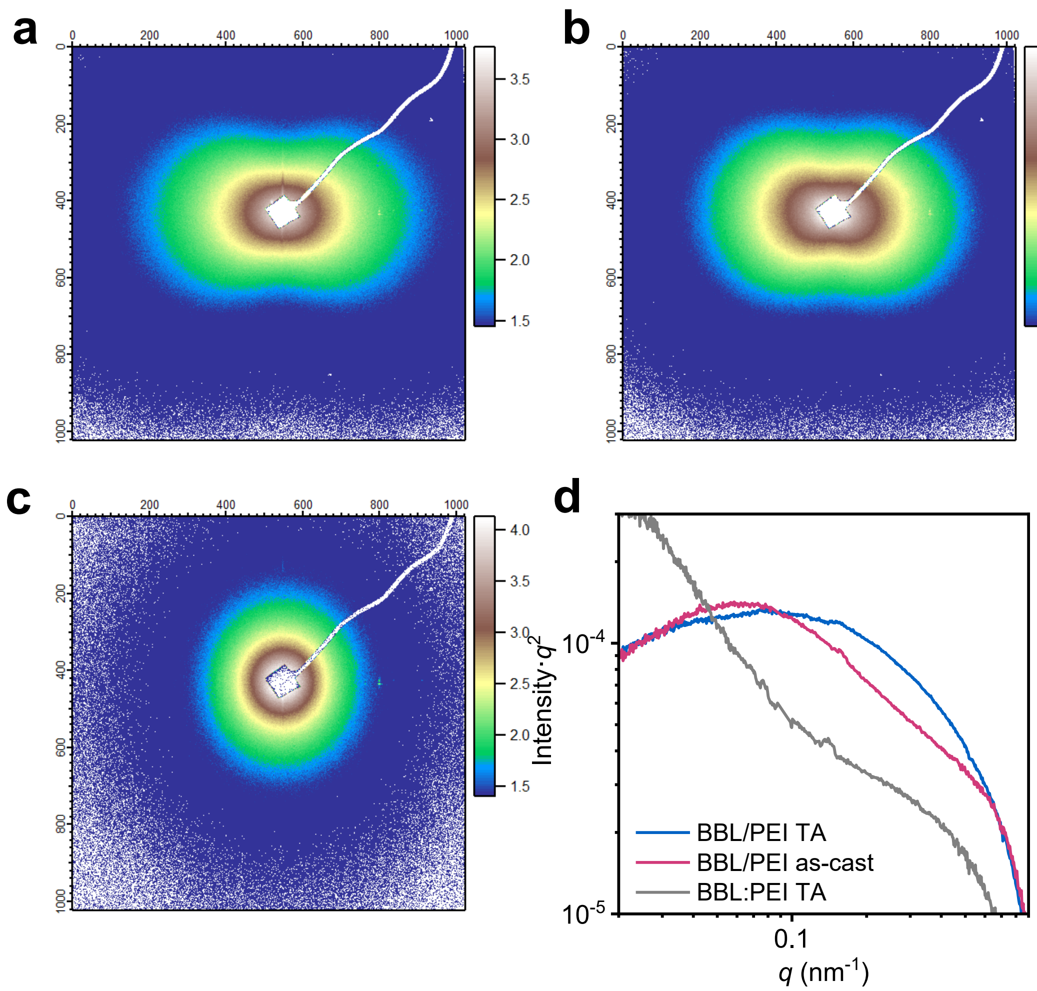

Fig. S9 | C-edge RSoXS. a-c, 2D R-SoXS images of a, thermal annealed BBL/PEI, b, as-cast BBL/PEI and c, thermal annealed BBL:PEI films, color legends denote the scattering intensity. d, 1D RSoXS profile of the films. q denotes the scattering vector. The data was fitted and summarized in **Table S4**.

Table S4 | Summary of the C-edge R-SoXS measurement.

Samples	q (nm^{-1})	Domain spacing (nm)	Domain Size (nm)	Horizontal intensity	Relative phase purity	Anisotropy
BBL/PEI TA	0.078	80.5	40.3	4.26E-08	1.00	0.49
BBL/PEI As-cast	0.059	106.4	53.2	3.46E-08	0.81	0.43
BBL:PEI TA	-	-	-	2.20E-08	0.52	0.15

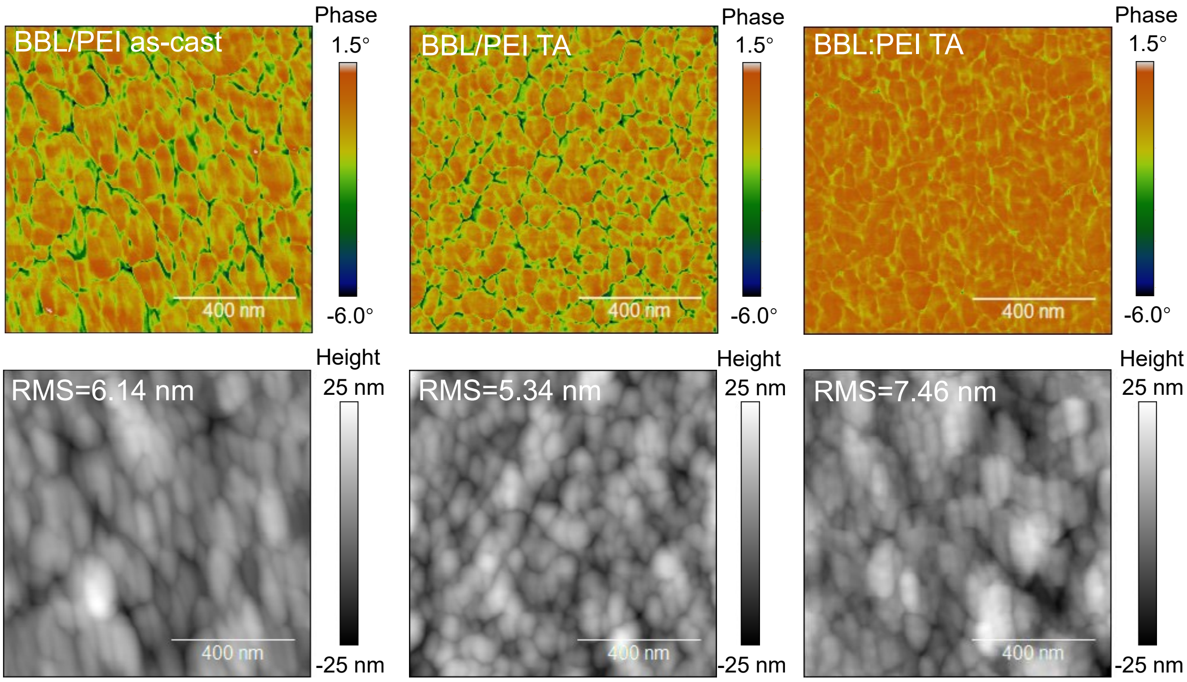

Fig. S10 | AFM phase (Top) image and height (Bottom) images of the blended films with and without GIBS. The sequential-deposited as-cast BBL/PEI film with GIBS shows obvious phase separation. After thermal annealing (TA), the domain spacing is reduced while the phase separation remains. This is consistent with the GIBS design principles, where the inter-mixing and continuous phase of PEI promotes ion transport while maintaining the BBL phase mostly continuous and undisrupted. In contrast, no phase separation can be observed for the blended BBL:PEI film, indicting the over-intermixed morphology. AFM measurement was successfully repeated for one time per condition. All AFM data are entirely consistent with the RSoXS results (see Fig. S9).

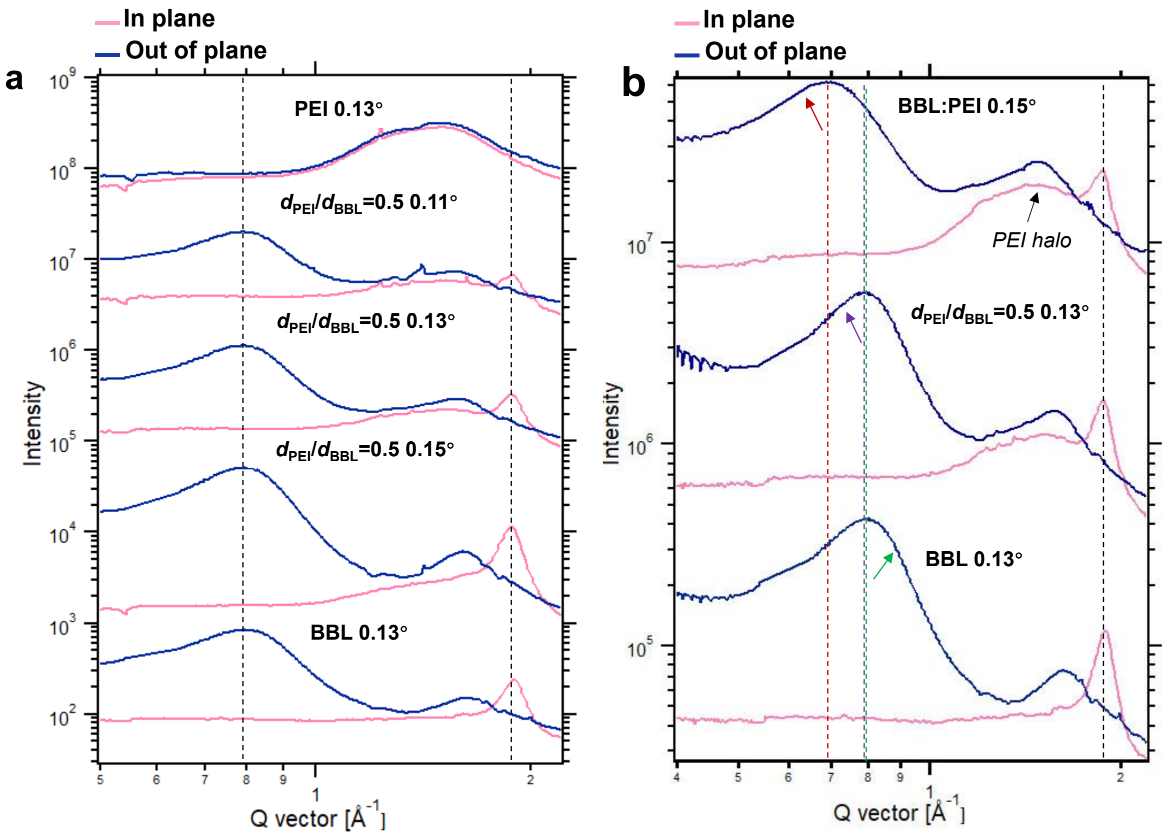

Fig. S11 | GIWAXS measurement. a, 1D GIWAXS profiles of the thermal annealed branched PEI, BBL and BBL/PEI films. For BBL/PEI film, the selected incident angles range from 0.11° to 0.15°, to evaluate the vertical distribution of BBL and PEI. b, 1D GIWAXS profile comparison of GIPS, BBL: PEI and BBL films. Blue and pink solid lines To uniform the PEI to BBL ratio in the test region, the weight ratio of BBL:PEI film and the thickness ratio of BBL/PEI film were selected as PEI/BBL=25% and PEI/BBL=50% respectively, and the incident angles of BBL: PEI and BBL/PEI films were selected as 0.15°and 0.13°respectively. In this case, the peak area ratio between the PEI halo and 010_{BBL} can be close, indicating a similar PEI to BBL ratio in the test area. The arrows and dashed lines guide the eyes to the peak center of the (100), (200) and (010) peaks (red: BBL:PEI, purple: BBL/PEI, green: BBL). The data was fitted and summarized in **Table S5**.

Table S5 | Summary of the GIWAXS measurement.

Sample		Location (Å^{-1})	d-spacing (Å)	FWHM (Å^{-1})	Coherence length (Å)	$S_{PEI}/S_{010\ BBL}$
BBL	010 (IP)	1.89	3.32	0.136	41.58	0
BBL/PEI 0.11°		1.88	3.34	0.125	45.24	8.41
BBL/PEI 0.13°		1.88	3.35	0.127	44.53	6.85
BBL/PEI 0.15°		1.88	3.35	0.132	42.84	4.50
BBL:PEI		1.87	3.36	0.138	40.98	6.59
BBL	100 (OOP)	0.799	7.86	0.220	25.47	-
BBL/PEI 0.11°		0.791	7.94	0.207	27.32	-
BBL/PEI 0.13°		0.791	7.94	0.211	26.80	-
BBL/PEI 0.15°		0.792	7.93	0.211	26.80	-
BBL:PEI		0.688	9.13	0.265	21.34	-

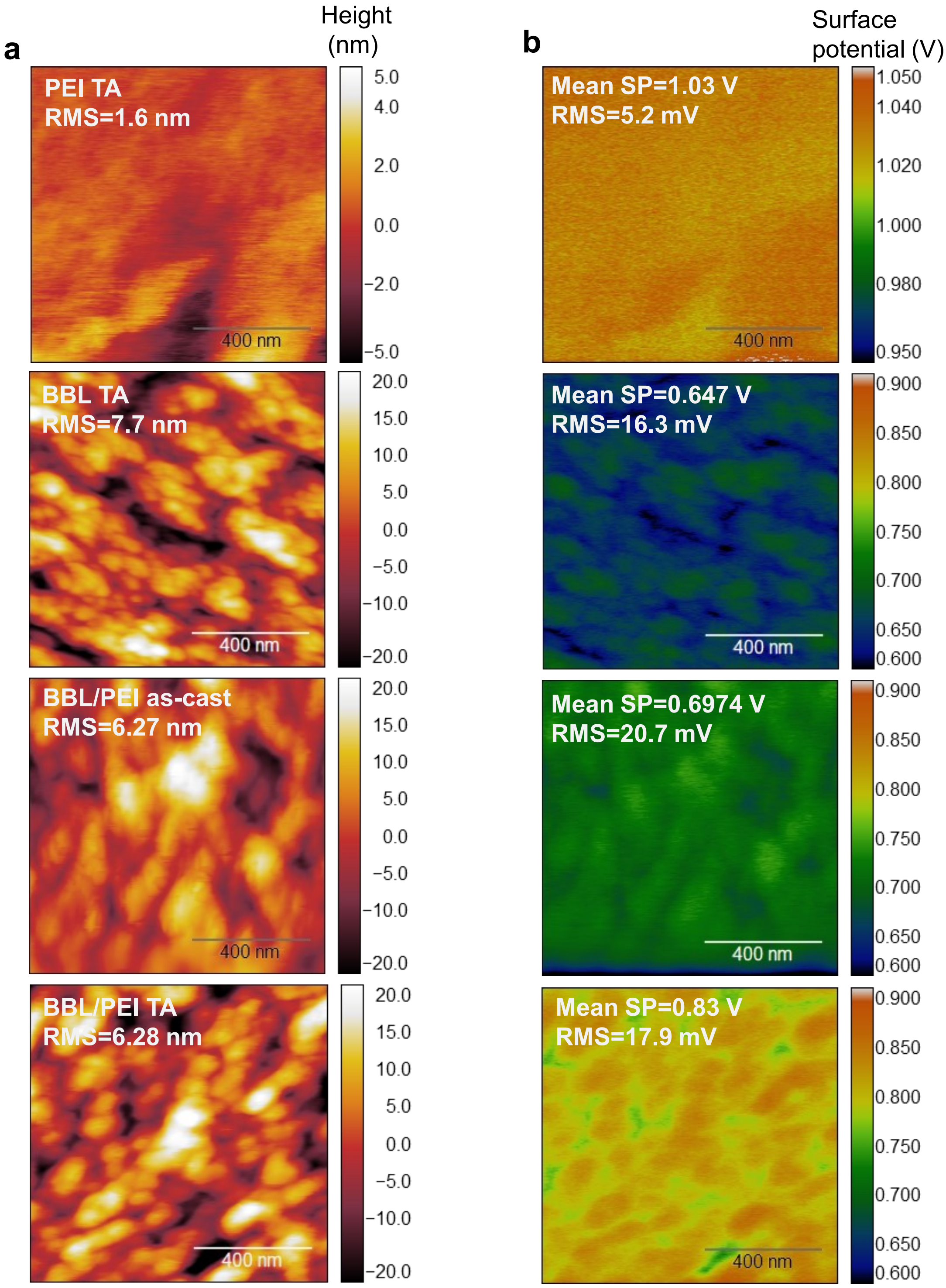

Fig. S12 | KPFM images. a, Topography and b**,** surface potential images of the samples. The electron-rich characteristic of the -NH_2 group facilitates the electron transfer from PEI to BBL upon thermal activation (thermal annealing, TA). This molecular *n*-doping effect lifts the Fermi level of BBL. Because the Fermi levels of the probe tip and the BBL sample are aligned during the KPFM test, this *n*-doping effect leads to an increase in the surface potential. Thus, the measured increase of surface potential can demonstrate the *n*-type doping of BBL. This experiment was successfully repeated for one time per condition.

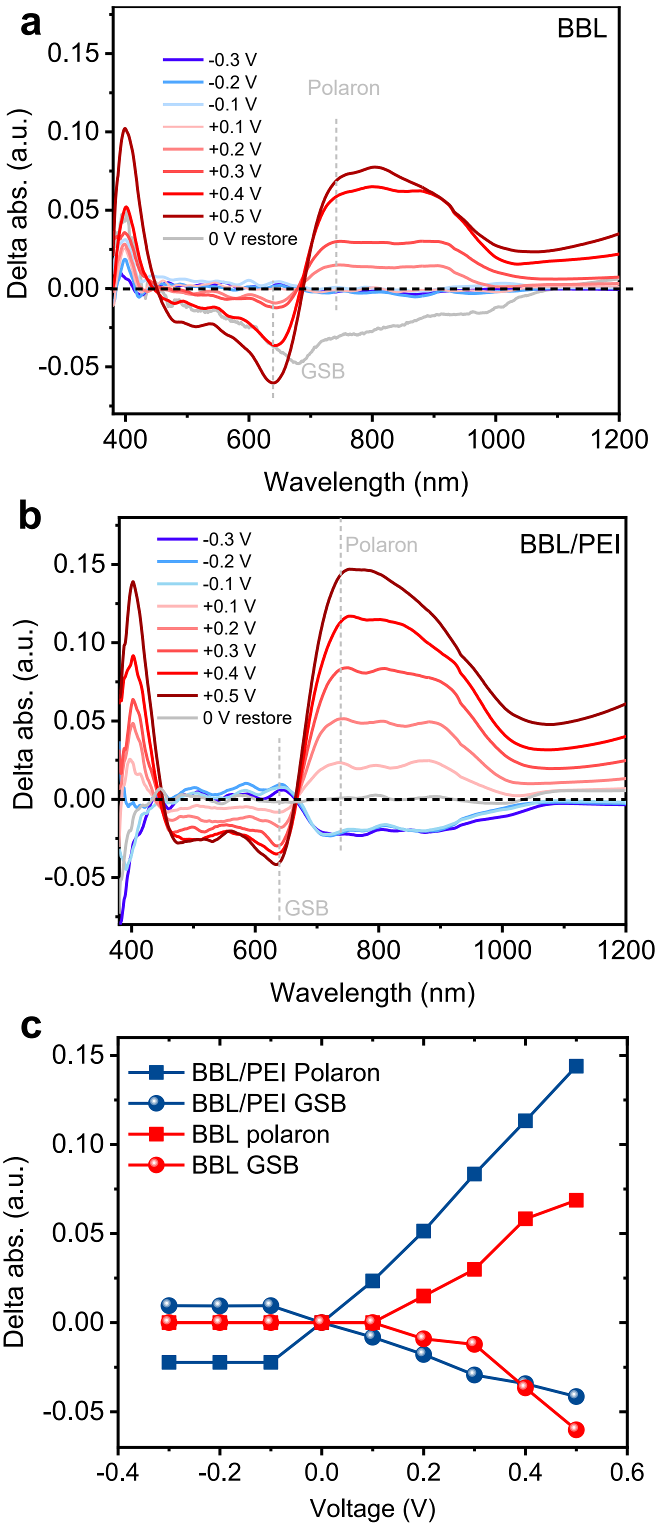

Fig. S13 | In-operando Uv-vis absorption measurement. a, 1D In-operando Uv-vis spectra of BBL film, and b, BBL/PEI film at different doping potential. Delta abs. denotes the different between the absorbance at doping potential and 0 V. c, Normalized GSB (at 630 nm) and polaron (at 740 nm) absorption intensity as functions of doping potential.

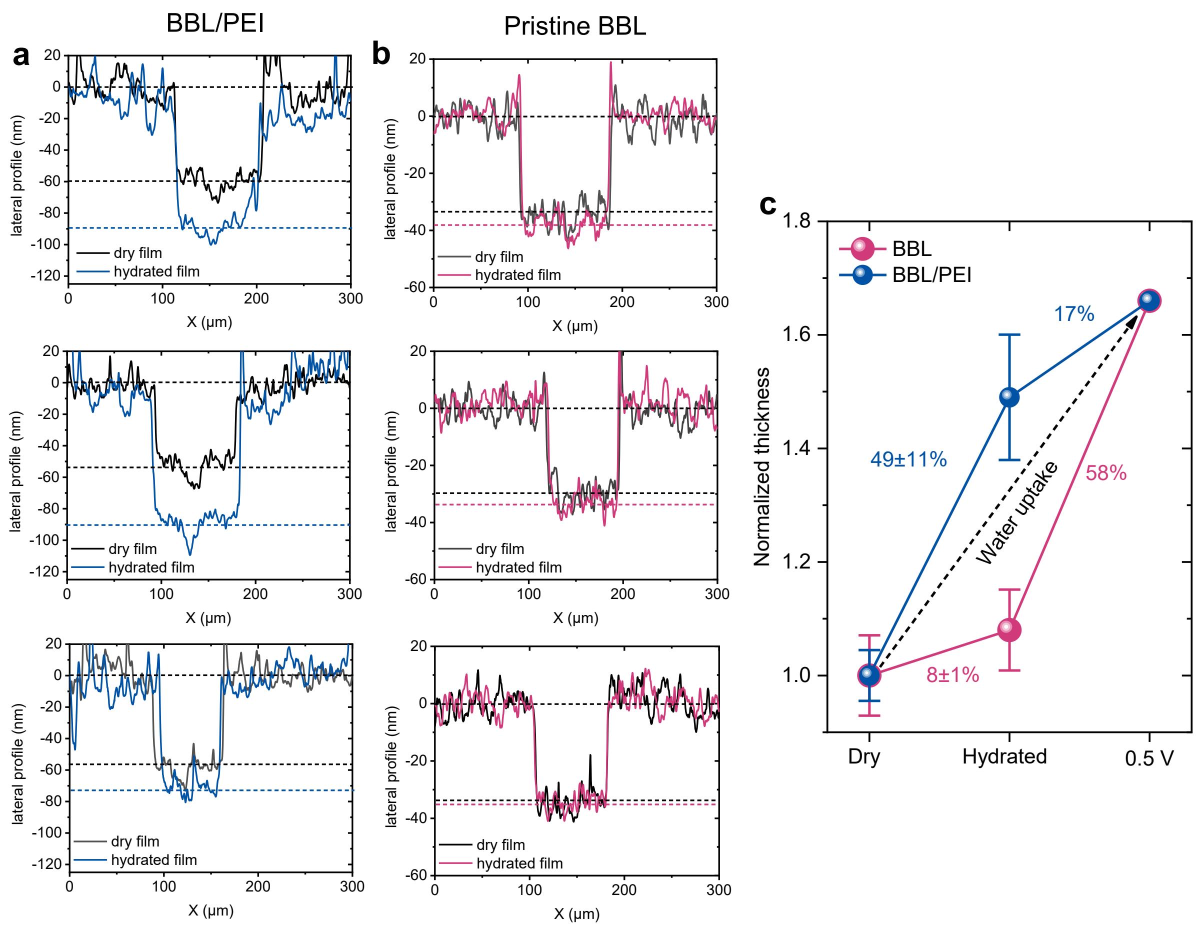

Fig. S14 | In-operando thickness measurement. a-b, Height profiles of three different cross sections on BBL/PEI and BBL films. c, Summaries of the swelling level of BBL and BBL/PEI films in different conditions (data are presented as mean ± s.d., error bars denote the s.d. for $n = 3$ different samples).

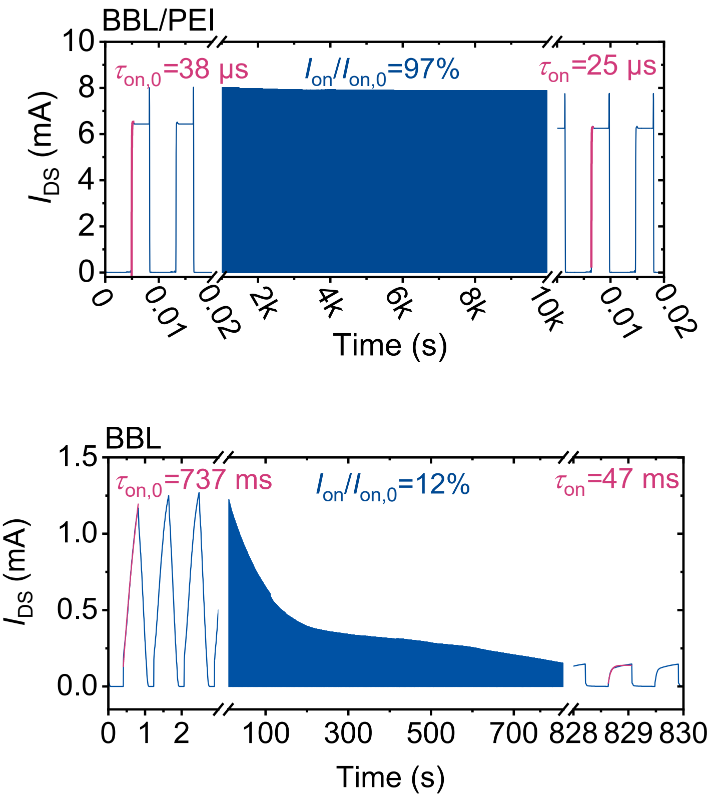

Fig. S15 | Switching stability of sv-OECT and BBL v-OECT tested in ambient environment. $I_{on,0}$ and I_{on} denote the on-state current before and after cycles, V_{DS} = 0.6 V, V_{GS} = ± 0.5 V.

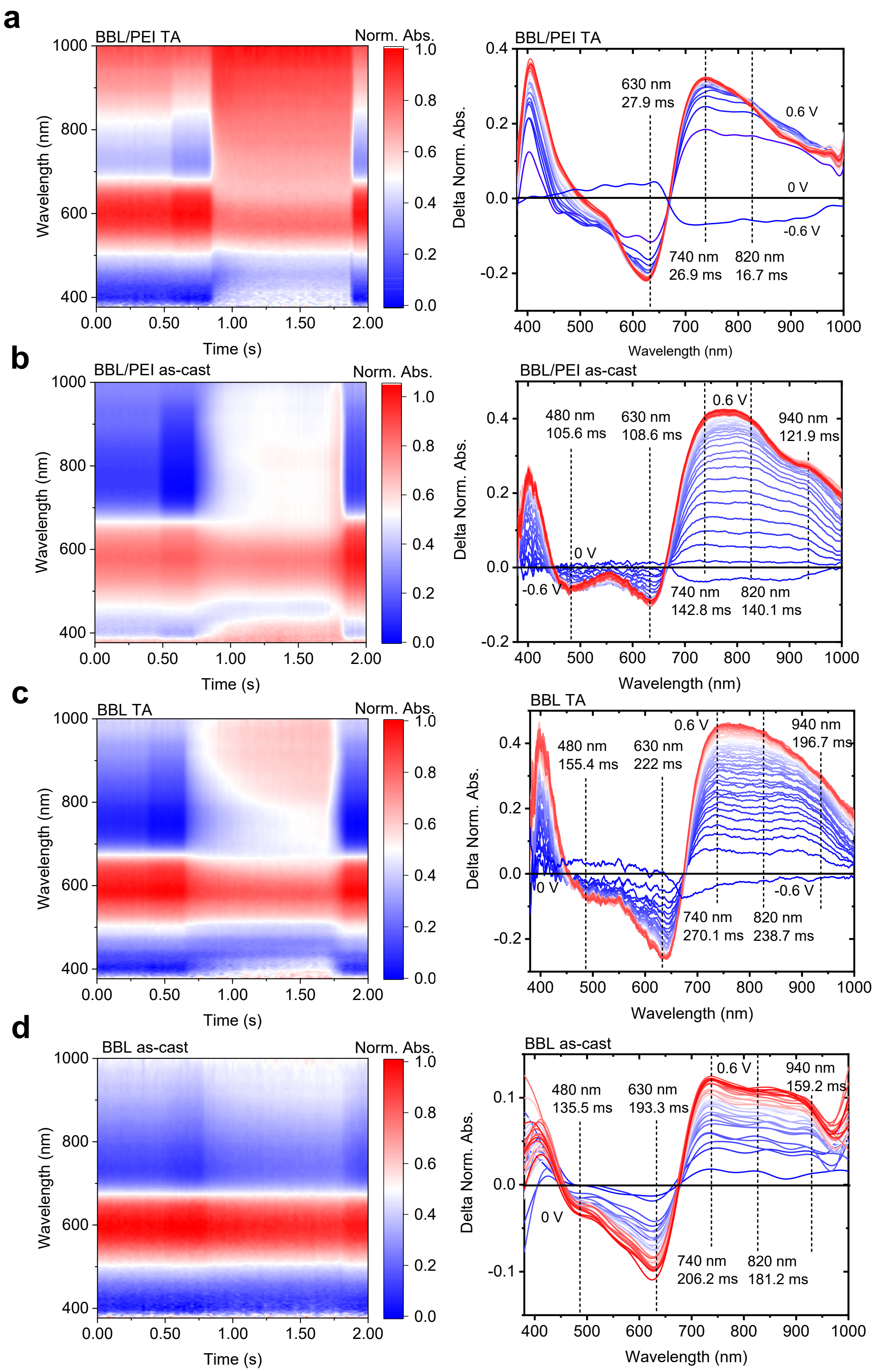

Fig. S16 | Time-resolved UV-vis absorption measurement. Norm. abs denotes the normalized absorbance. Delta Norm. abs. denotes the different between the normalized absorbance at doping potential and 0 V.

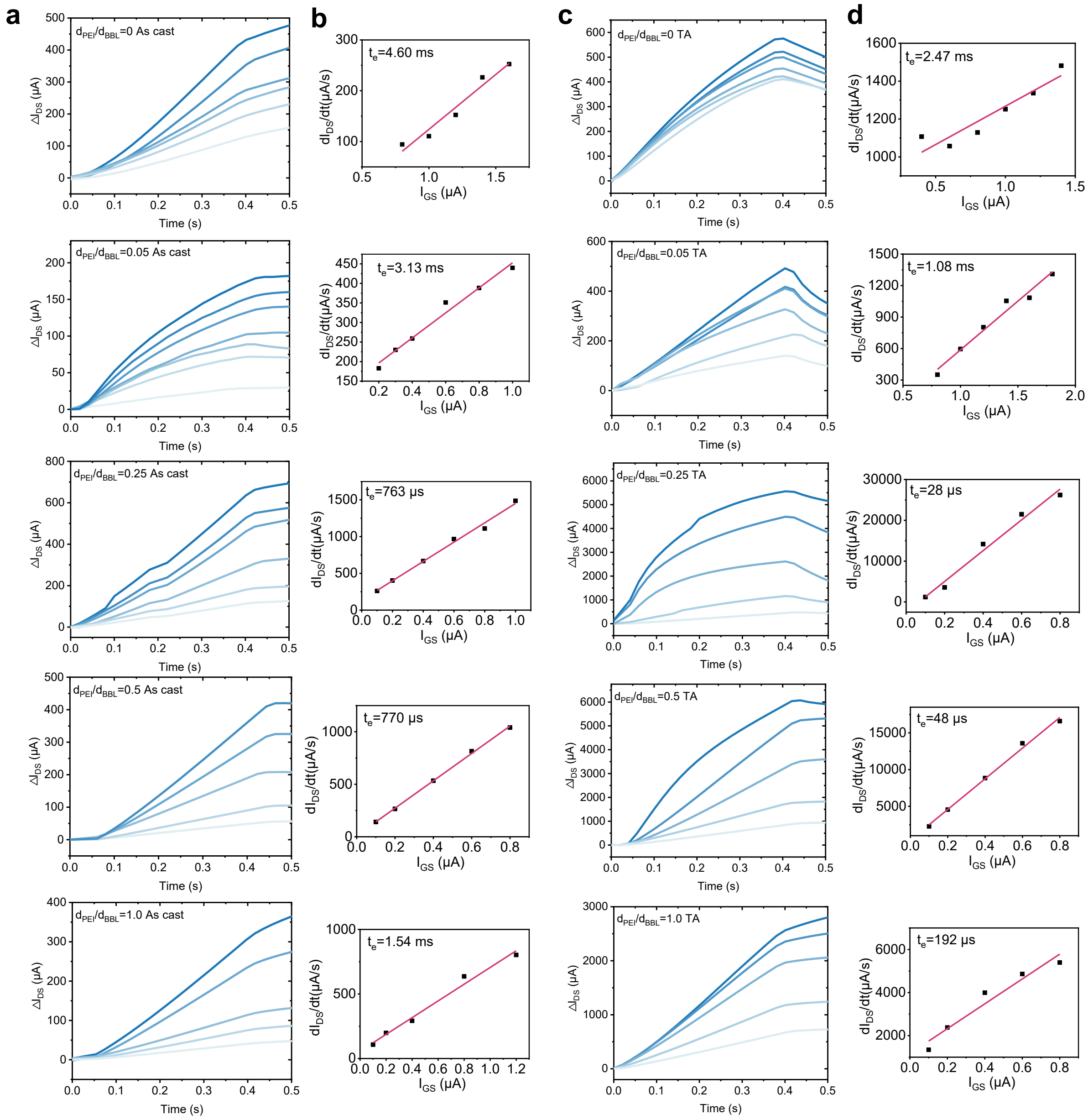

Fig. S17 | Measurement of electron transit time (τ_e) in sv-OECTs. a and c, The temporal I_{DS} response of as-cast a, and thermal annealed c, BBL/PEI-based sv-OECTs upon I_{GS} pulse with different amplitude, ΔI_{DS} denotes the difference between real-time drain current and initial drain current. b and d, The corresponding plot and linear fit of $\partial I_{DS}/\partial t$ versus I_{GS} pulse amplitude, black squares and red solid lines are raw data and fitted data, respectively.

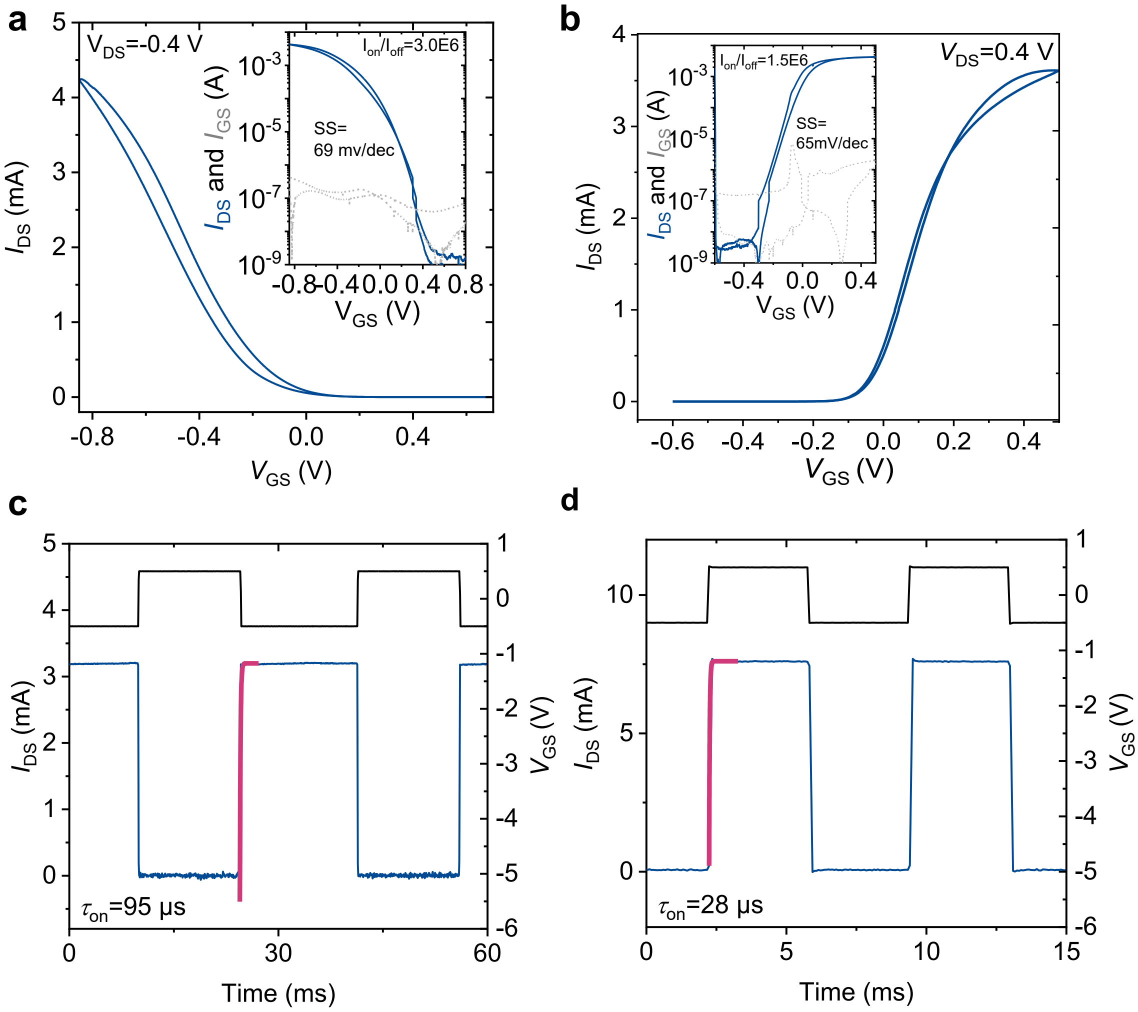

Fig. S18 | Performances of *n*/*p*-type OECTs for complementary amplifier. a, Transfer curves of a, *n*-type BBL/PEI-based sv-OECT and b, *p*-type PTBT-P-based v-OECT. Insets are logarithmic transfer curves. Dashed lines are gate current, Subthreshold swing ($SS=dV_{GS}/d[\log_{10}(I_{DS})]$) and on/off ratio ($I_{on}/I_{off}$) are also showed. c-d Transient response of c, *p*-type PTBT-P-based v-OECTs and d, *n*-type BBL/PEI-based sv-OECT upon ± 0.5 V V_{GS} pulses. Blue and red lines denote the raw and fitted data, respectively.

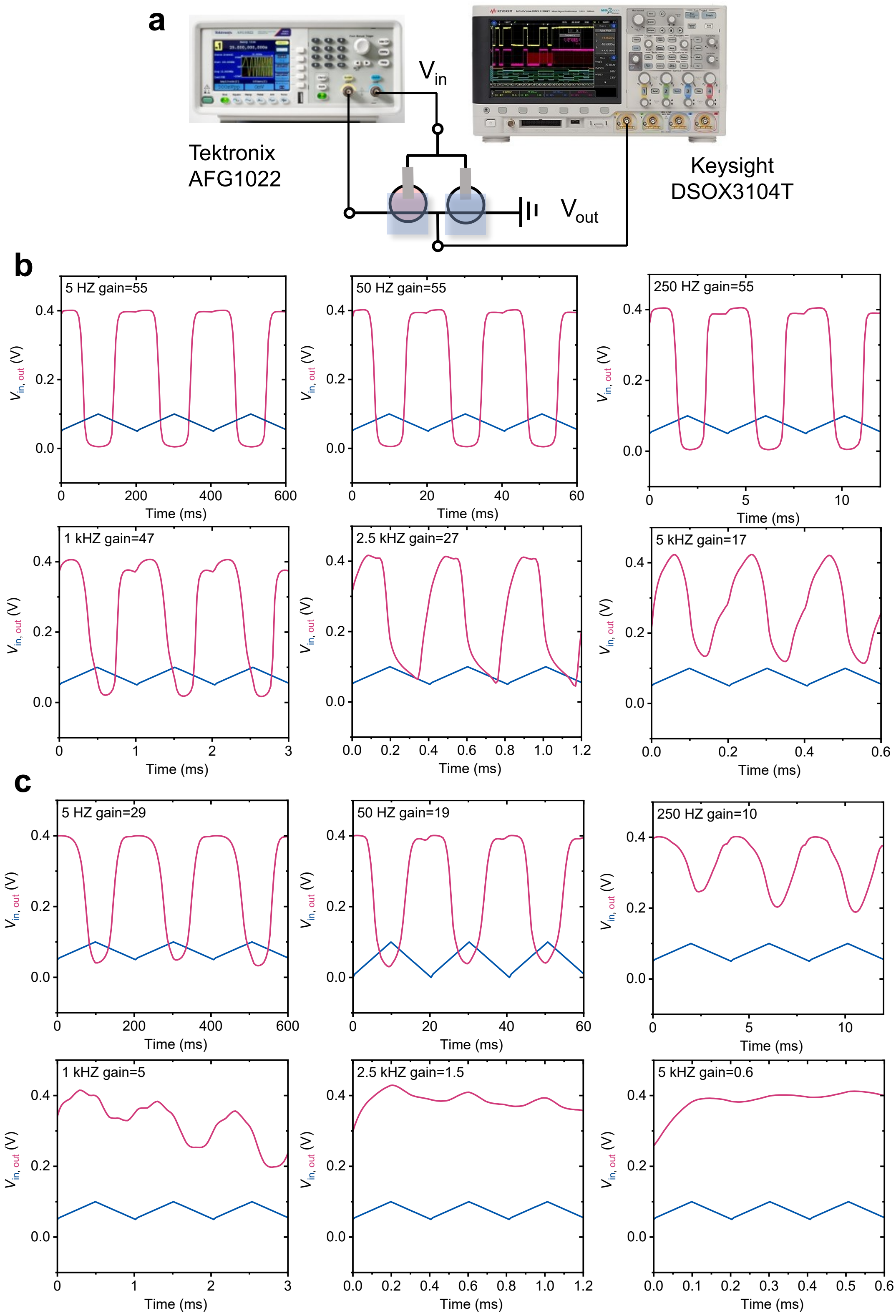

Fig. S19 | Amplification capability of BBL/PEI- and BBL-based complementary amplifier. a, Experiment setup. b-c, Triangular input (V_{in} = 0.05~0.1 V with the frequency of 5~5000 Hz and V_{DD} = 0.4 V) with the corresponding amplified output.

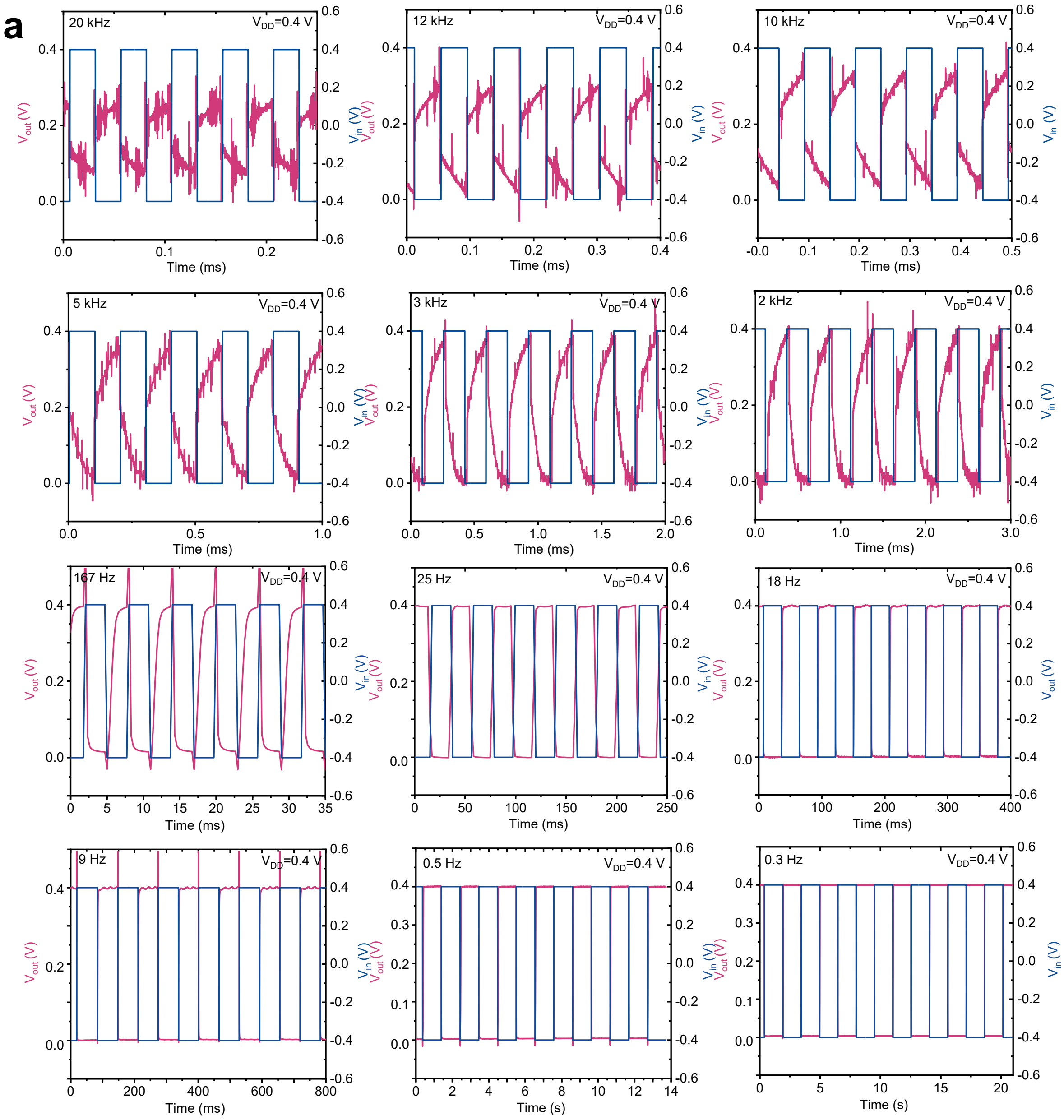
a
20 kHz
12 kHz
10 kHz
5 kHz
3 kHz
2 kHz
167 Hz
25 Hz
18 Hz
9 Hz
0.5 Hz
0.3 Hz
VDD=0.4 V
Vout (V)
Vin (V)
Time (ms)
Time (s)

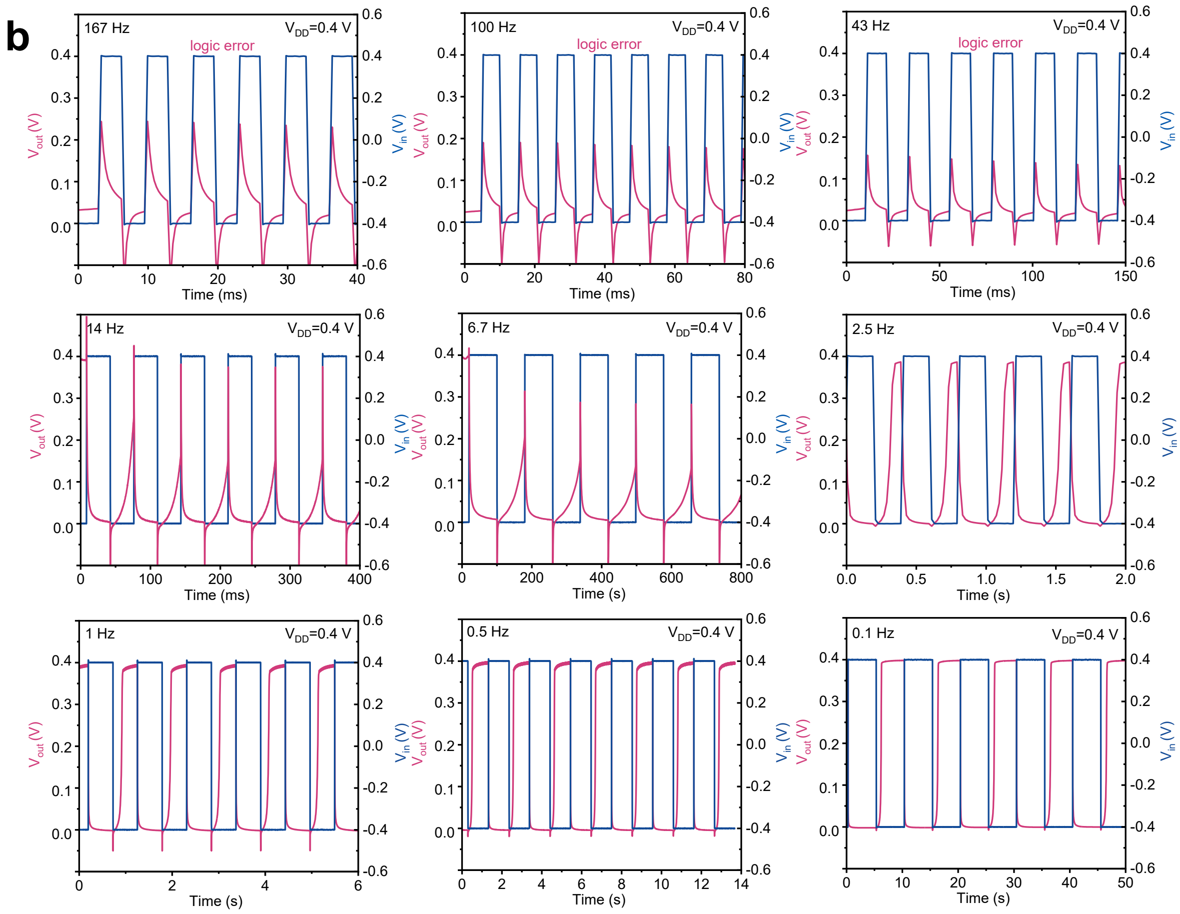

Fig. S20 | Output response of BBL/PEI- and BBL-based amplifier with pulsed input. a-b, Output response of a, BBL/PEI-based and b, BBL-based amplifier at different input frequency.

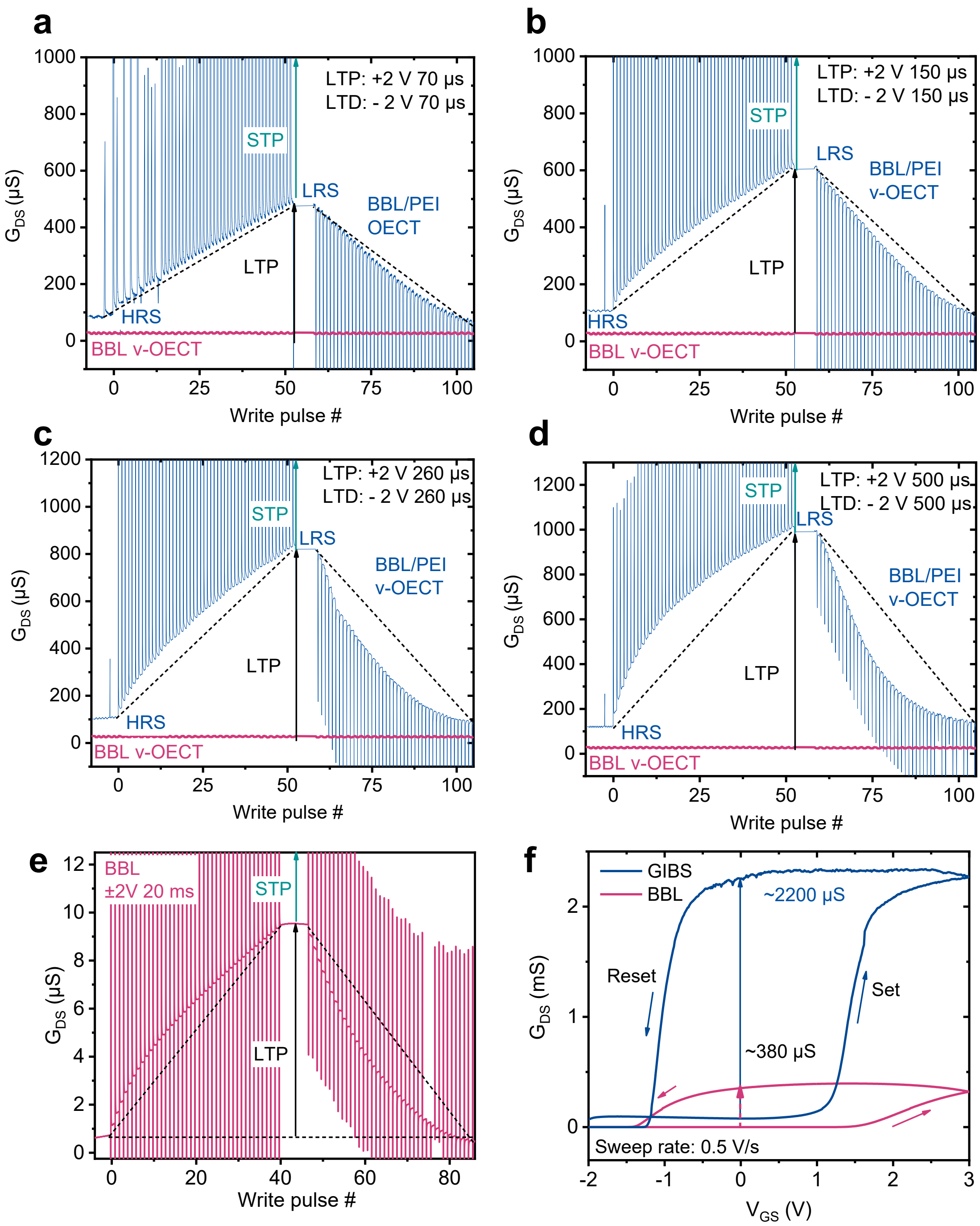

Fig. S21 | Performance of BBL/PEI- and BBL -based ECRAMs. a-e, Short-term potentiation/depression (STP/STD) and long-term potentiation/depression (LTP/LTD) behavior of BBL/PEI-based and BBL-based ECRAMs controlled by gate voltage pulses with different pulse widths. Black and green arrows guide the eyes to LTP and STP traces, respectively. Black dashed lines guide the eye to the conductance update during LTP/LTD. f, Transfer curves BBL/PEI- and BBL-based ECRAMs (gated by EMIMTFSI ion gel and Au electrode).

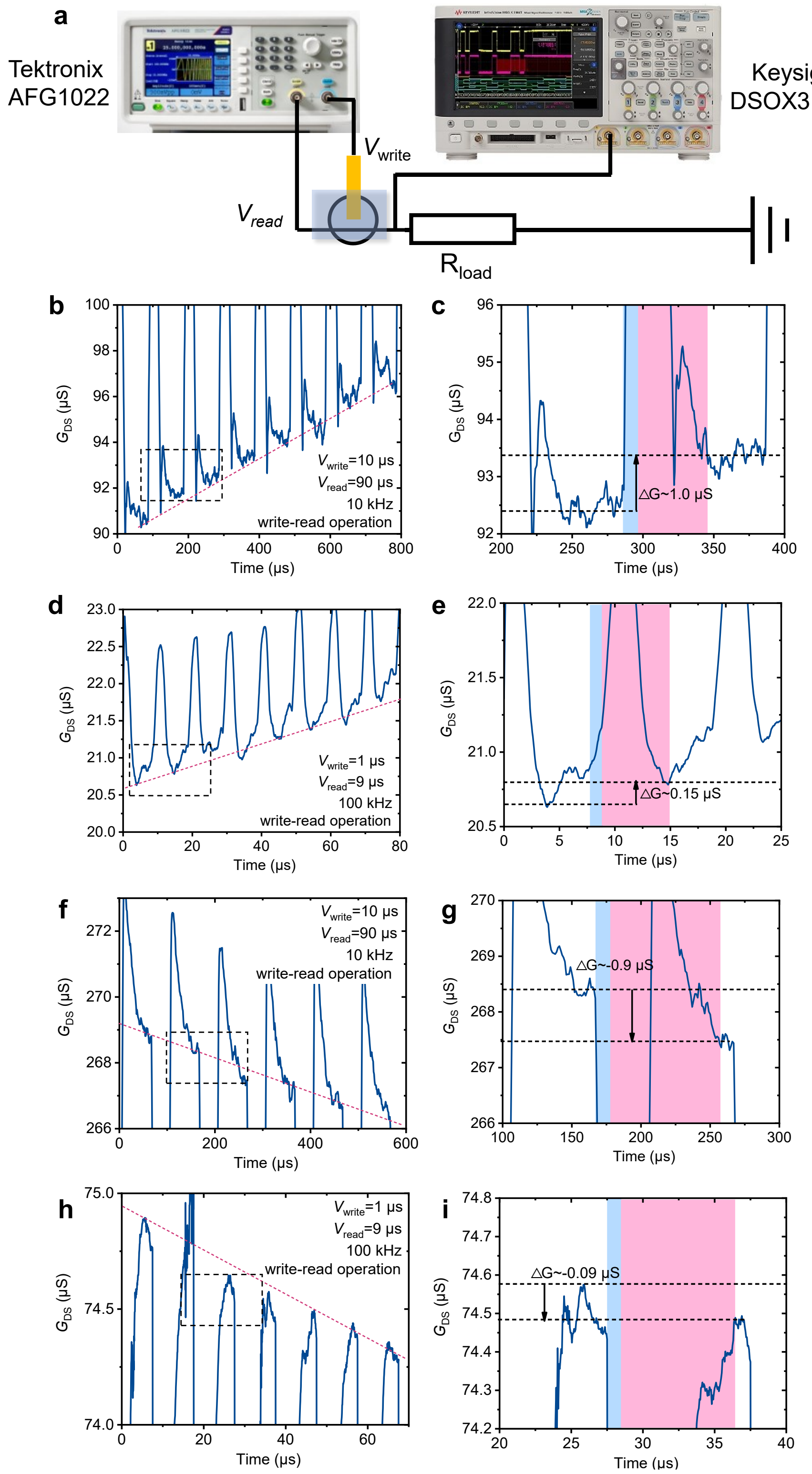

Fig. S22 | High-frequency write-read operation on BBL/PEI-based ECRAMs. a, Experiment setup. V_{write} and V_{read} denote the write/read voltage. b-e, Long-term potentiation of BBL/PEI-based ECRAMs at 10 kHz and 100 kHz. c and e are the enlarged images of the dashed box area of b and d, respectively. f-h, Long-term depression of BBL/PEI -based ECRAMs at 10 kHz and 100 kHz. g and i are the enlarged images of the dashed box area of f and h, respectively. For all the figures, pink dashed lines guide the eye to the conductance update traces. Black arrows and dashed lines guide the eye to the conductance update between two adjacent pulses. Blue and pink shadings represent the write and read stage, respectively.

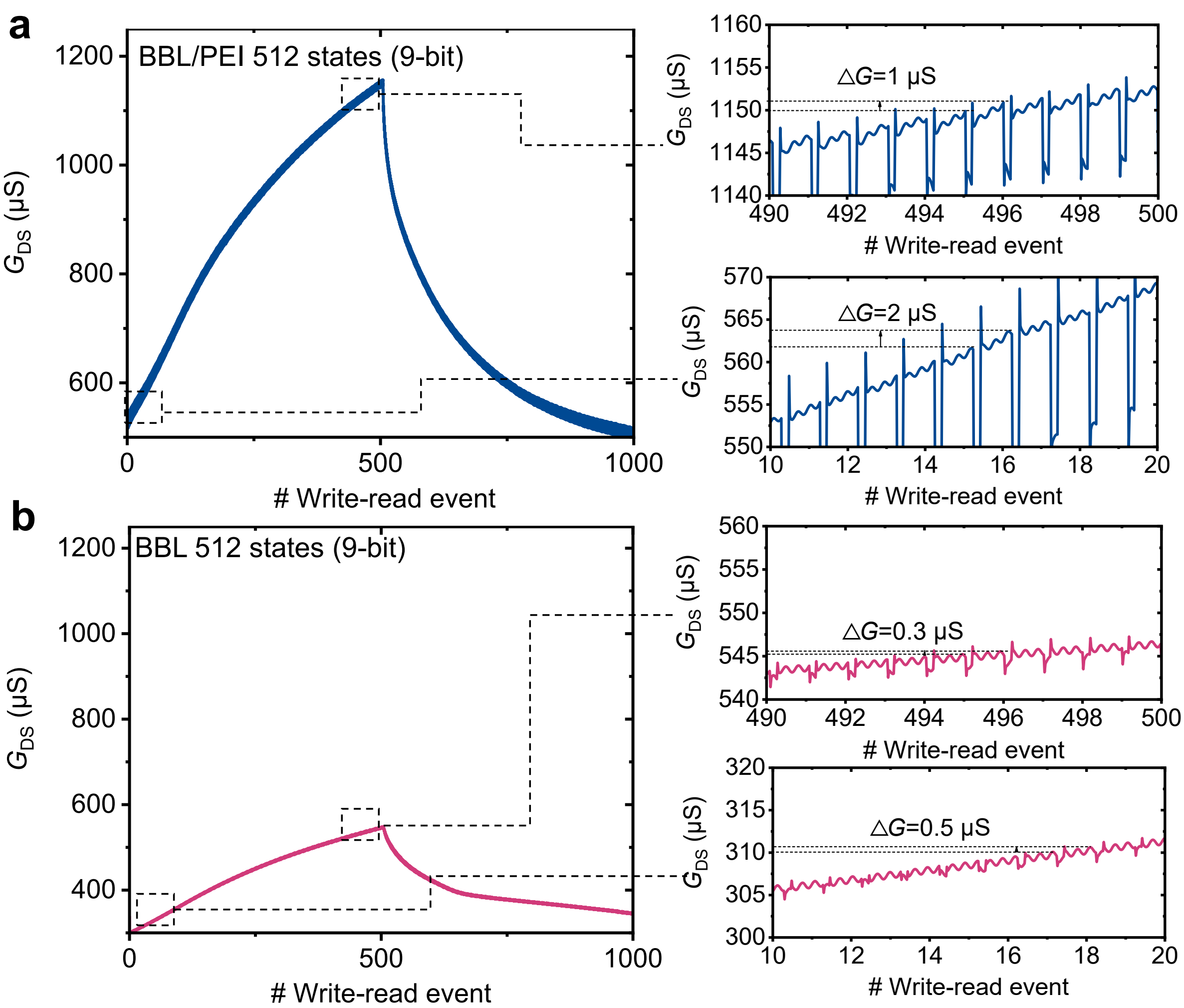

Fig. S23 | LTP/LTD behavior of ECRAMs with 512 conductance states (9-bit). The right panels show the conductance update at the initial and final stage (dased box) of the LTP. +2 V, 10 μs (LTP, first 512 pulses)/-2 V, 10 μs (LTP, last 512 pulses) write pulses followed by 0.1 V, 90 μs read pulses were used for LTP/LTD measurement of BBL/PEI -based ECRAMs. +2 V, 20 ms (LTP, first 512 pulses)/-2 V, 20 ms (LTP, last 512 pulses) write pulses followed by 0.1 V, 180 ms read pulses were used for LTP/LTD measurement of BBL-based ECRAMs. Black arrows and dashed lines guide the eye to the conductance update between two adjacent pulses.

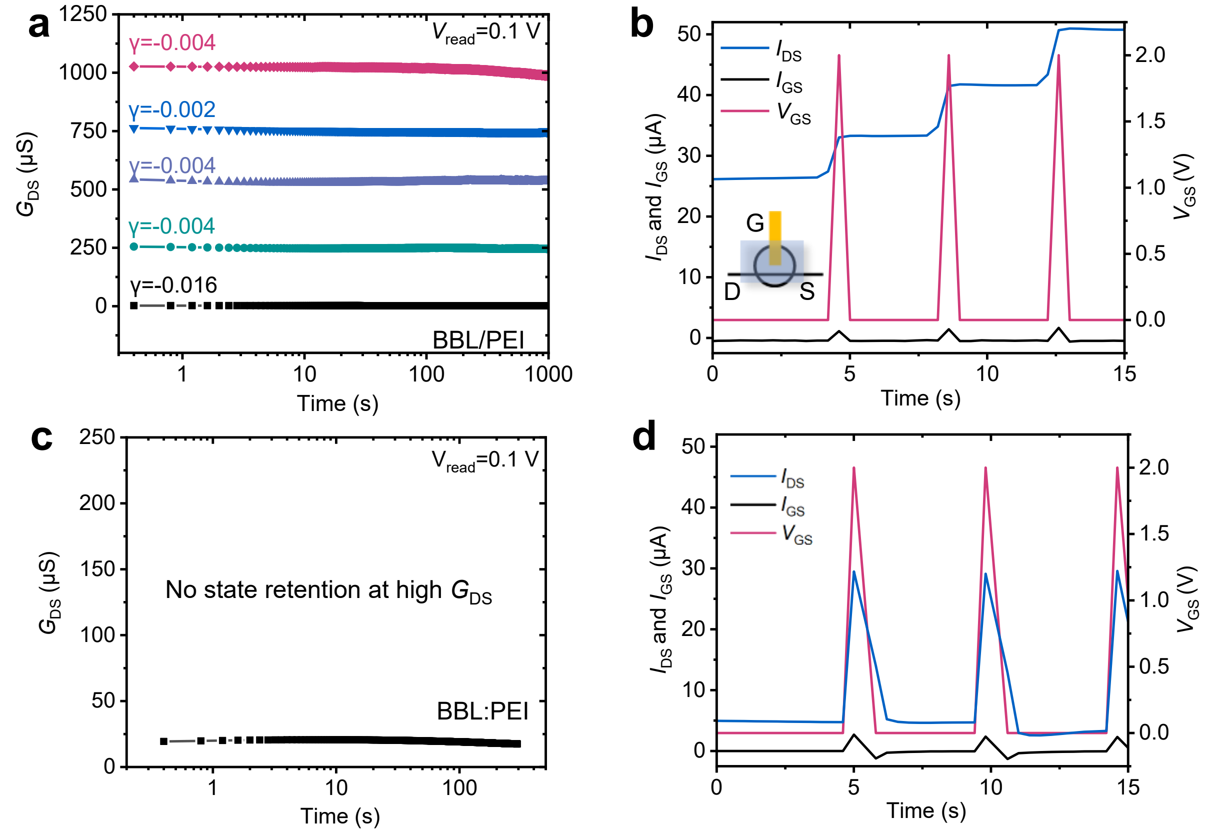

Fig. S24 | Non-volatile performance comparison of the BBL/PEI-based and BBL:PEI-based ECRAMs. a-b**,** State-retention a, and its training process b, of BBL/PEI-based ECRAM. c-d, State-retention c, and its training process d, of BBL:PEI-based ECRAM. The drift coefficients (γ) are calculated by equation: $G_{DS}(t) = G_{DS,0}(t/t_0)^{\gamma}$, where $G_{DS,0}$ is the initial conductance, t is the testing time

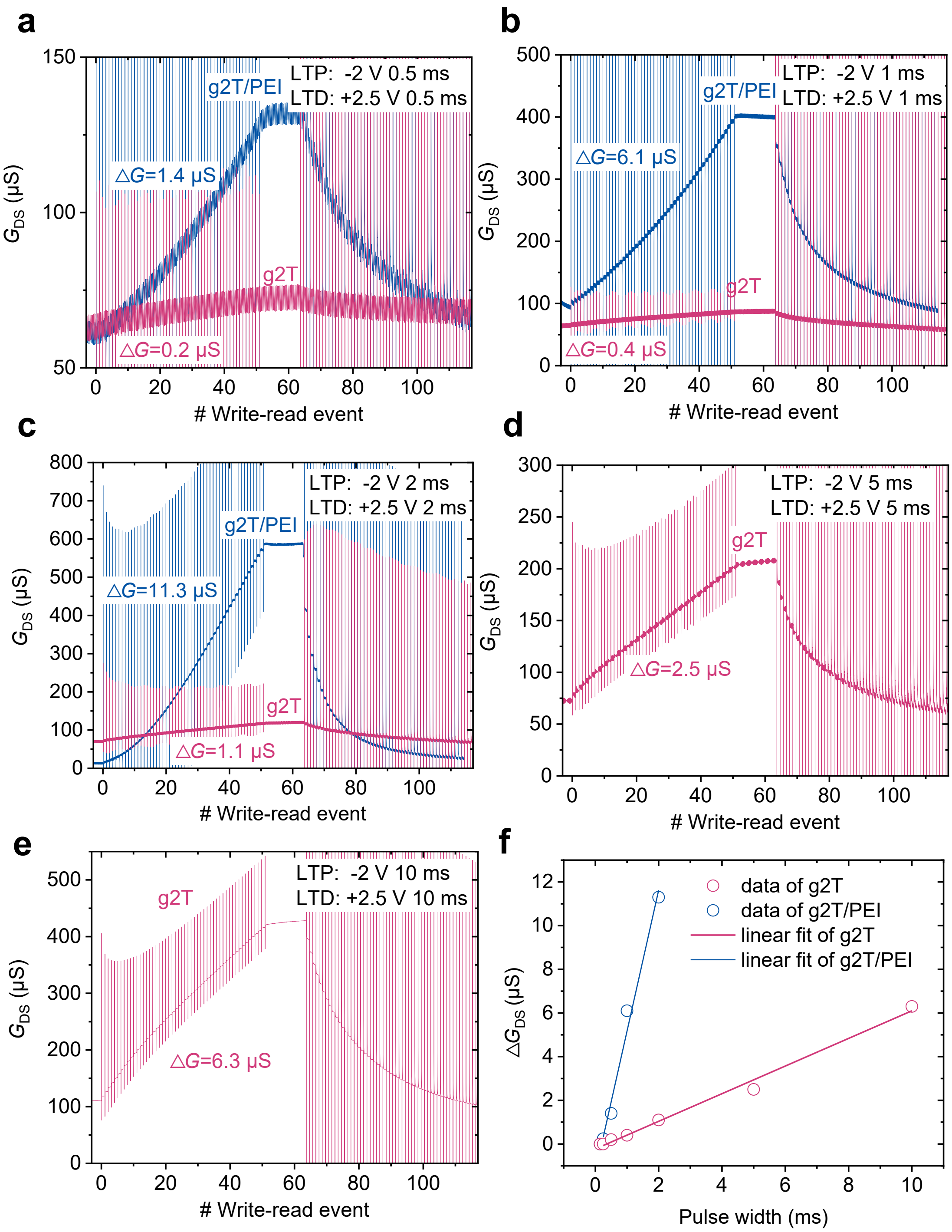

Fig. S25 | LTP/STP behavior of g2T-based and g2T/PEI-based ECRAMs. a-e, LTP and STP behavior controlled by gate voltage pulses with different pulse widths. f, Non-volatile conductance update as a function of gate voltage pulse width.

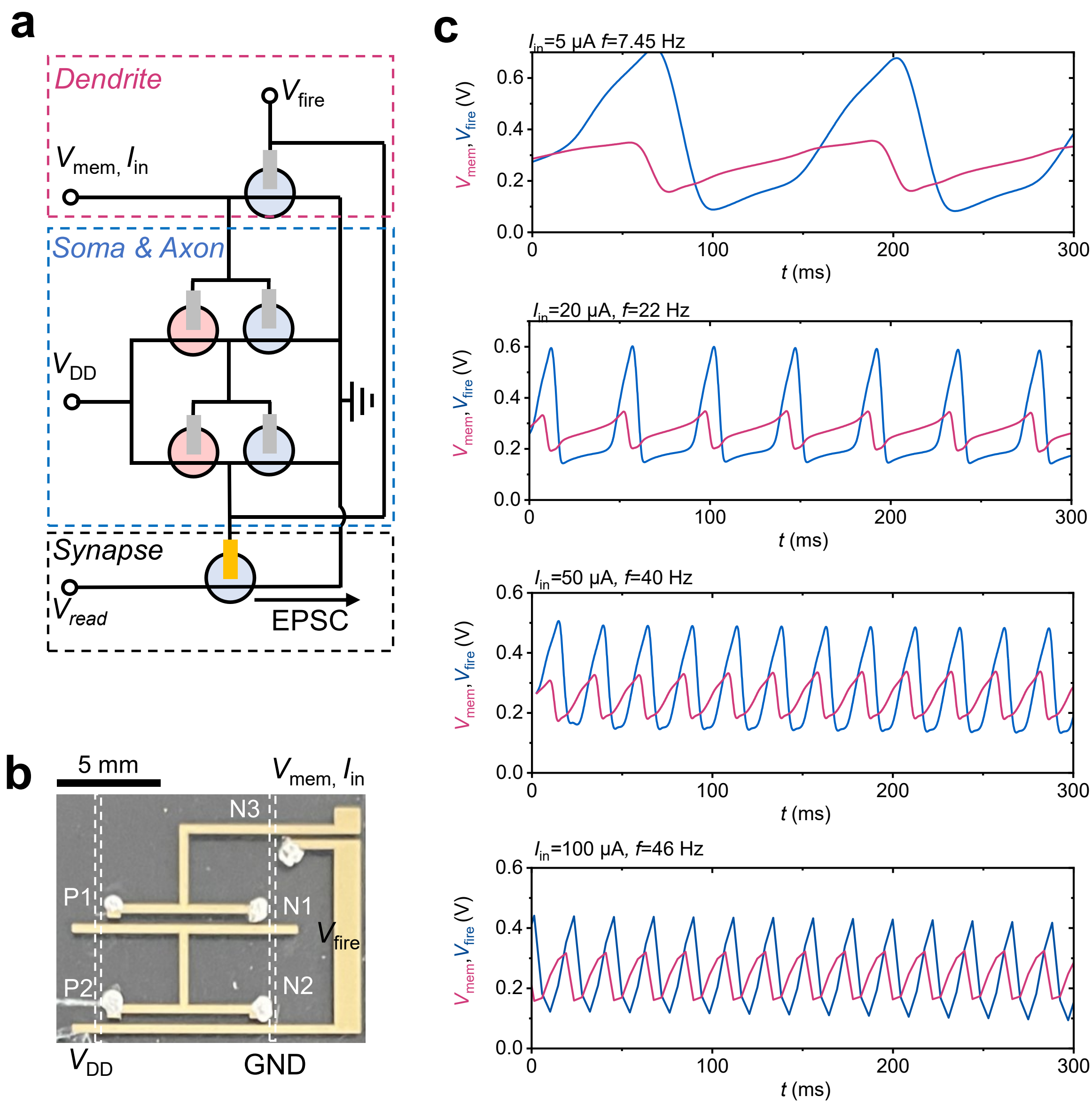

Fig. S26 | Sv-OECT based Axon-Hillock circuit for frequency encoding. a, Circuit diagram, where *p*-/*n*-type OECTs are based on PTBT-P (pink shading) and BBL/PEI (blue shading). V_{DD}, V_{fire}, V_{mem}, I_{in} and V_{read} denote the supply voltage, input voltage, fire voltage, membrane potential, input current and read voltage, respectively. b, Photograph of the circuit, where P1, P2 and N1-N3 represent *p*- and *n*-type OECTs. The white dashed boxes show the area of indium tin oxide drain electrodes. c, Typical spiking behavior with different input current (I_{in}) amplitude, *f* denotes the fire frequency.

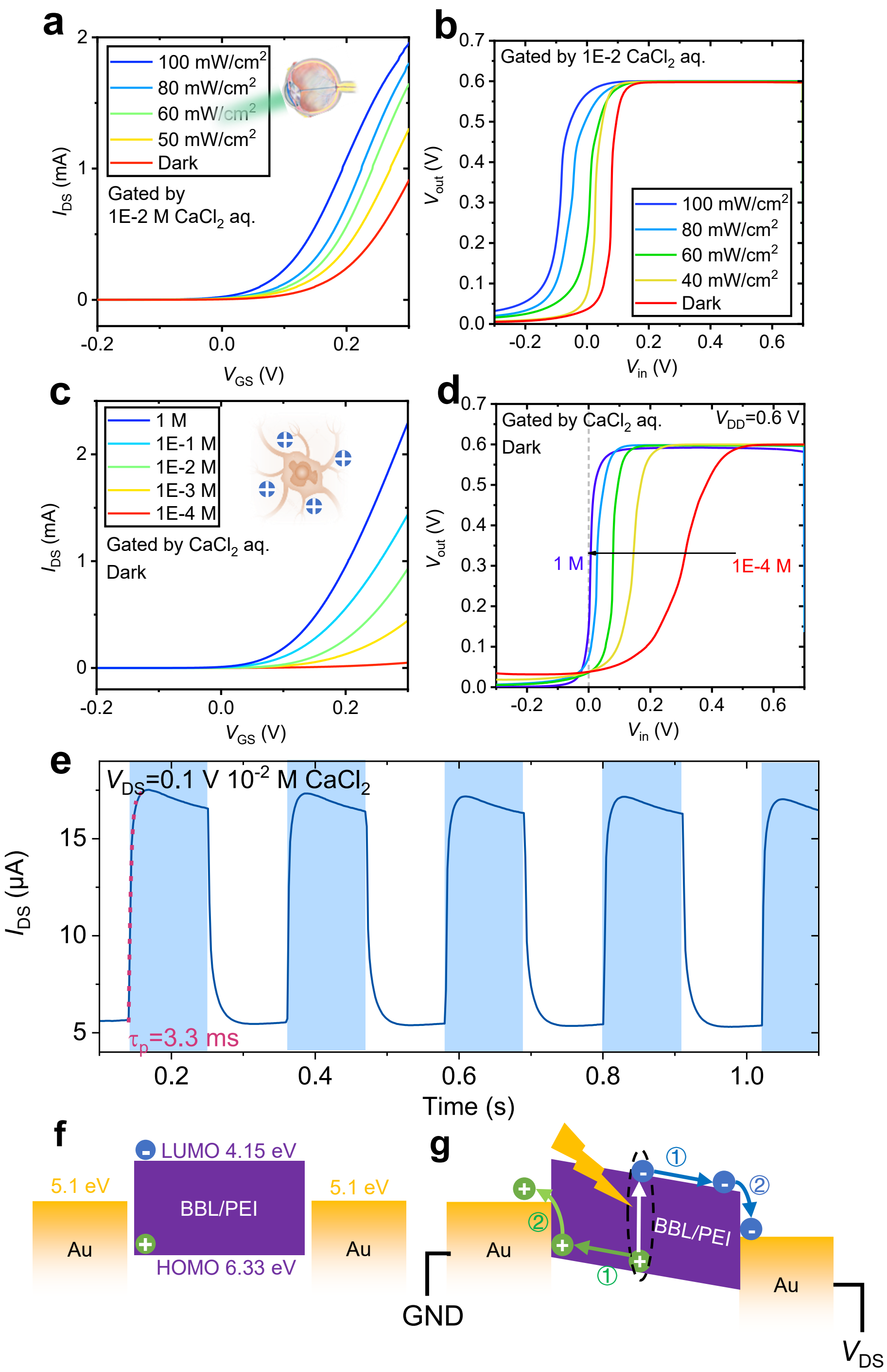

Fig. S27 | Light response of sv-OECT receptor. a, Transfer curves of sv-OECT receptor and b, membrane potential (V_{mem}) of sv-OECT-based soma amplifier under different light intensity (455 nm). c, Transfer curves of sv-OECT receptor and d, V_{mem} curves of soma amplifier under different Ca^{2+} concentration. e, Transient I_{DS} response of sv-OECT receptor upon light stimuli (455 nm, 100 mW, V_{DS}=0.1 V, V_{GS} = 0 V, blue shadings indicate the light on stage). f-g, Possible mechanism of light response, this process including ① exciton dissociation and charge transport in virtue of V_{DS} bias, and ② charge collection at Drain and Source. It is important to note that the dielectric constant of BBL (up to 8.2) [31] and PEI (up to 9) [32] can be much higher than the common organic semiconductors (ε_r~2-4), which may be important for the self-dissociation of excitons.

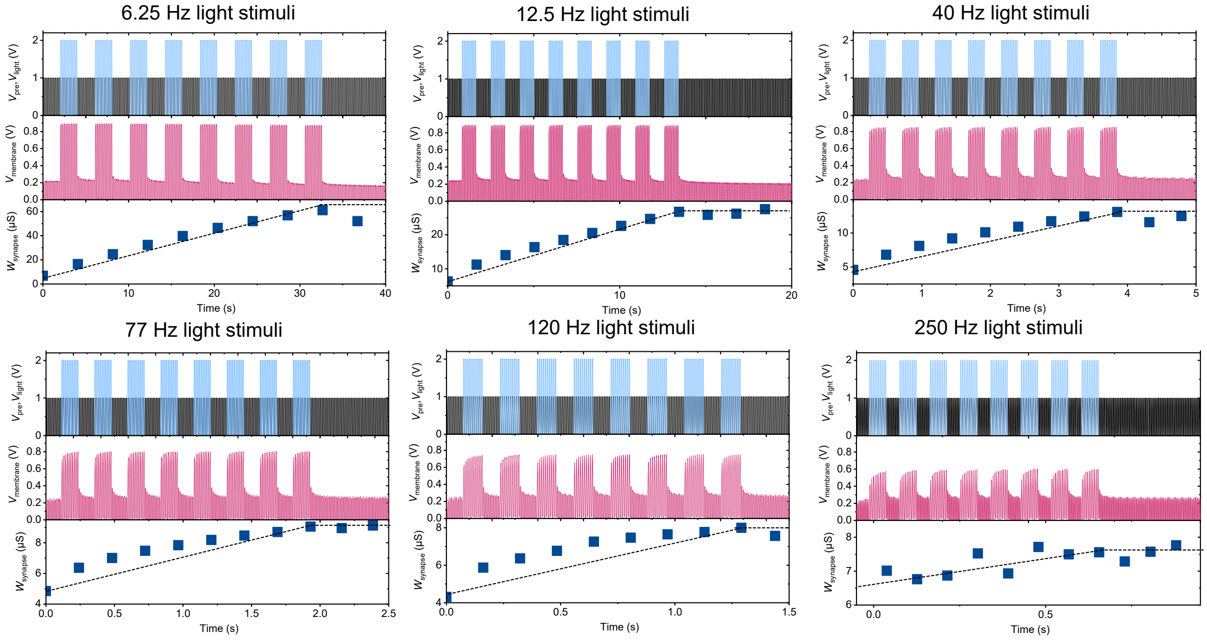

Fig. S28 | Real-time V_{mem} and W_{syn} response of BBL/PEI-based CMAN upon light stimuli (455nm, 100 mW/cm^2) at a Ca^{2+} concentration of 10^{-1} M. Dashed lines guide the eye to the trace of weight update.

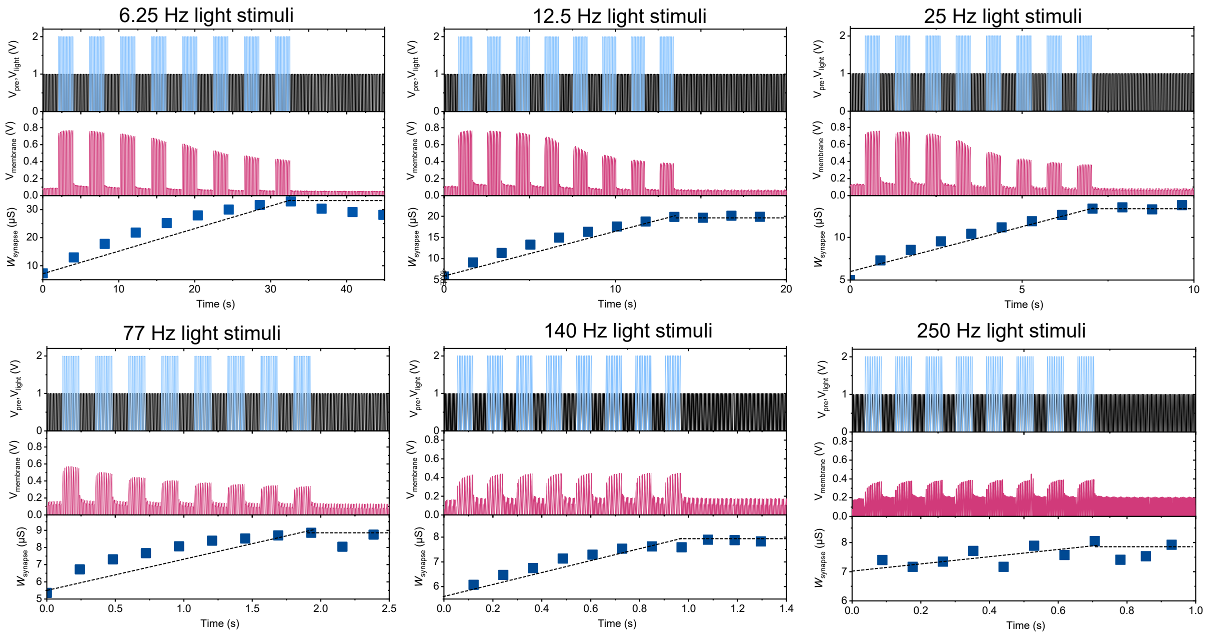

Fig. S29 | Real-time V_{mem} and W_{syn} response of BBL/PEI-based CMAN upon light stimuli (455 nm, 100 mW/cm^2) at the Ca^{2+} concentration of 10^{-2} M. Dashed lines guide the eye to the trace of weight update.

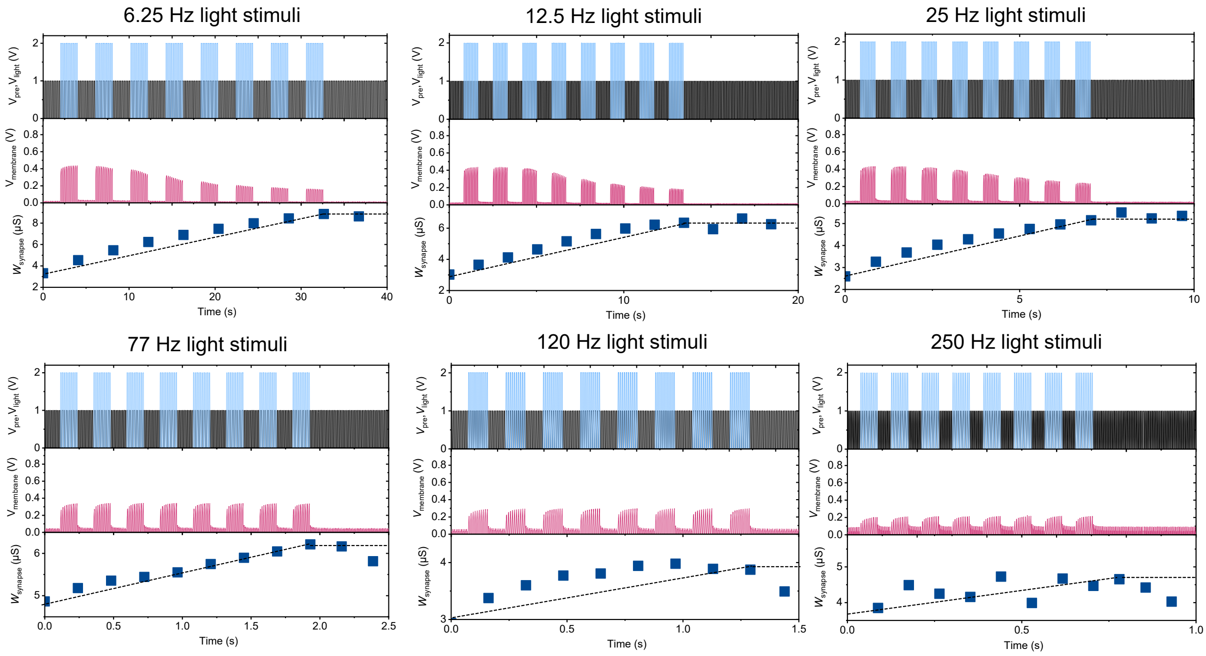

Fig. S30 | Real-time V_{mem} and W_{syn} response of BBL/PEI-based CMAN upon light stimuli (455nm, 100 mW/cm^2) at a Ca^{2+} concentration of 10^{-3} M. Dashed lines guide the eye to the trace of weight update.

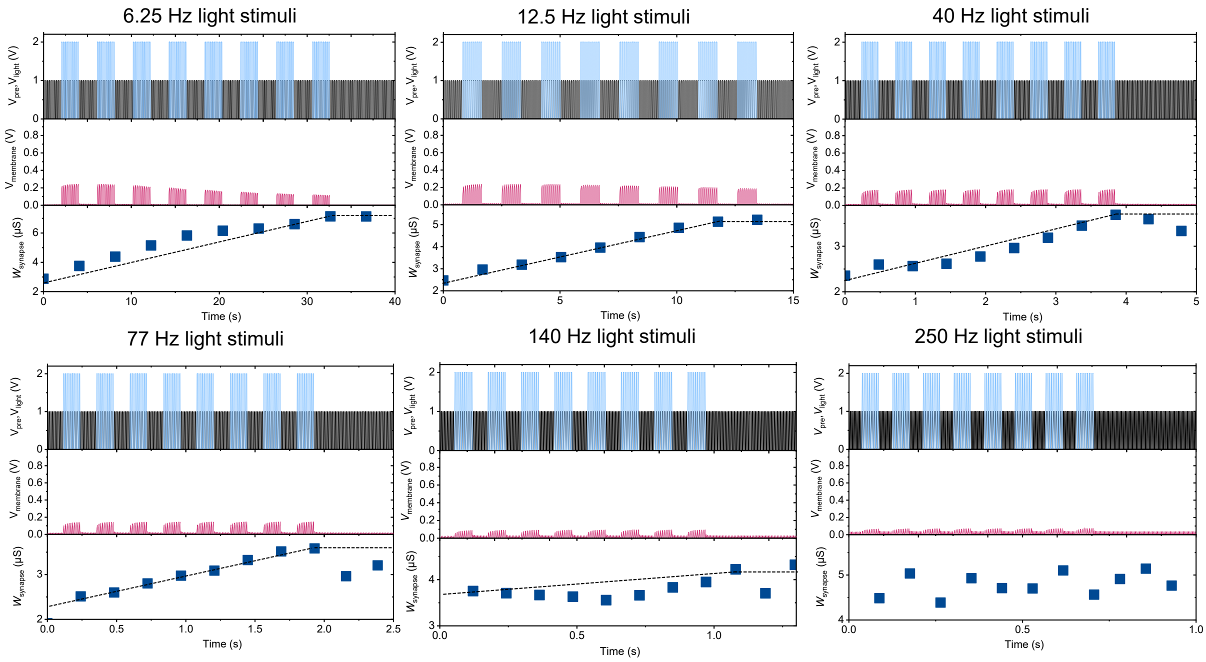

Fig. S31 | Real-time V_{mem} and W_{syn} response of BBL/PEI-based CMAN upon light stimuli (455 nm, 100 mW/cm^2) at a Ca^{2+} concentration of 10^{-4} M. Dashed lines guide the eye to the trace of weight update.

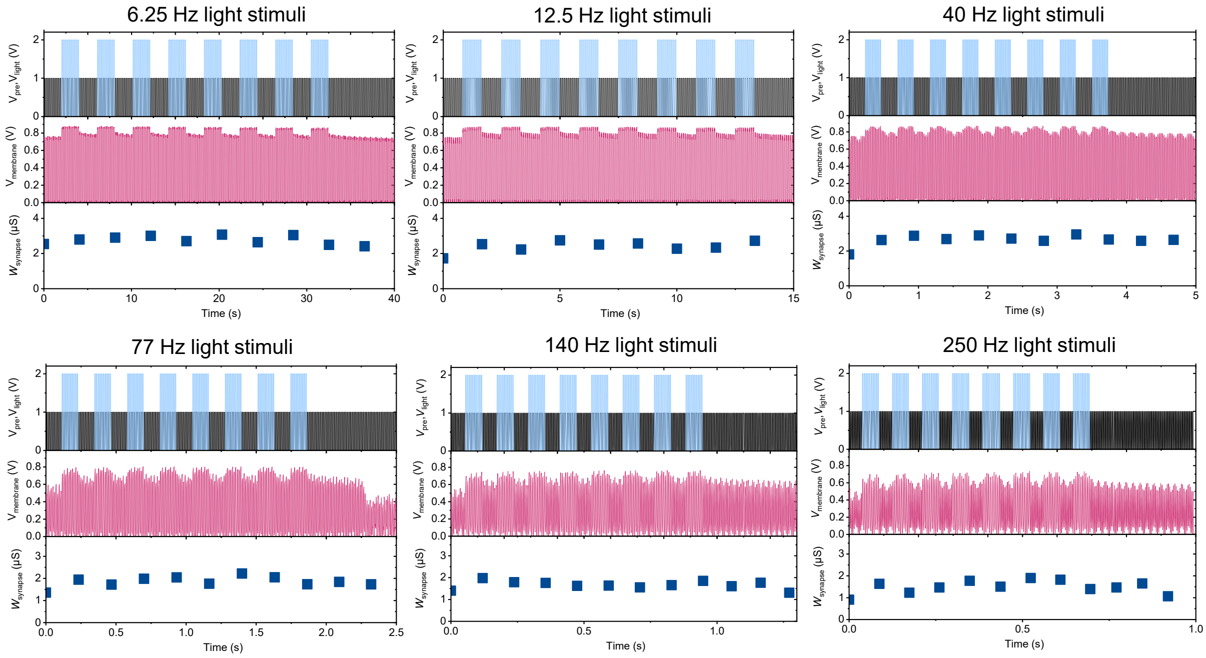

Fig. S32 | Real-time V_{mem} and W_{syn} response of BBL-based CMAN upon light stimuli (455 nm, 100 mW/cm^2) at a Ca^{2+} concentration of 10^{-1} M.

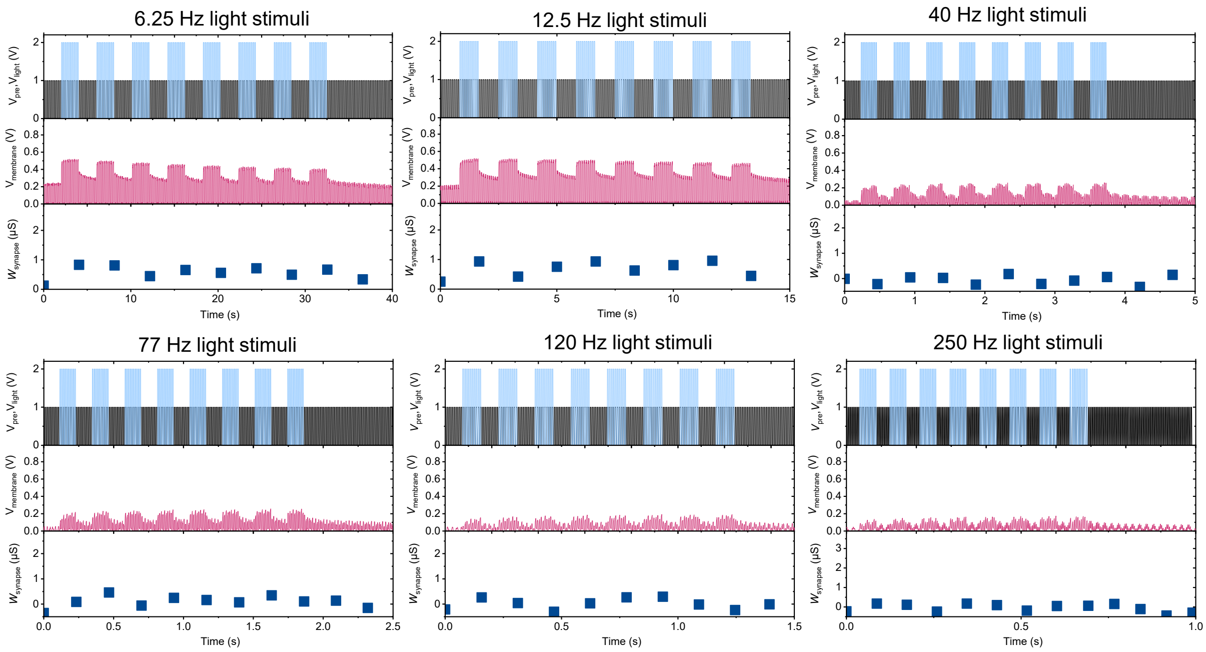

Fig. S33 | Real-time V_{mem} and W_{syn} response of BBL-based CMAN upon light stimuli (455 nm, 100 mW/cm^2) at a Ca^{2+} concentration of 10^{-2} M.

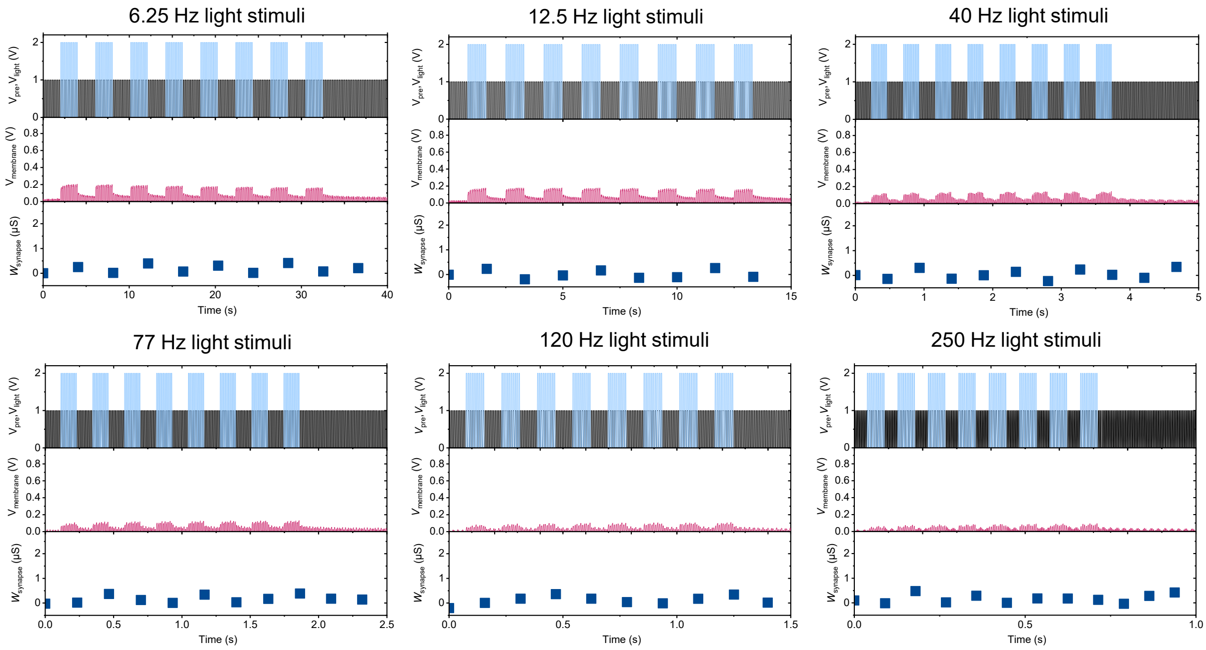

Fig. S34 | Real-time V_{mem} and W_{syn} response of BBL-based CMAN upon light stimuli (455 nm, 100 mW/cm^2) at a Ca^{2+} concentration of 10^{-3} M.

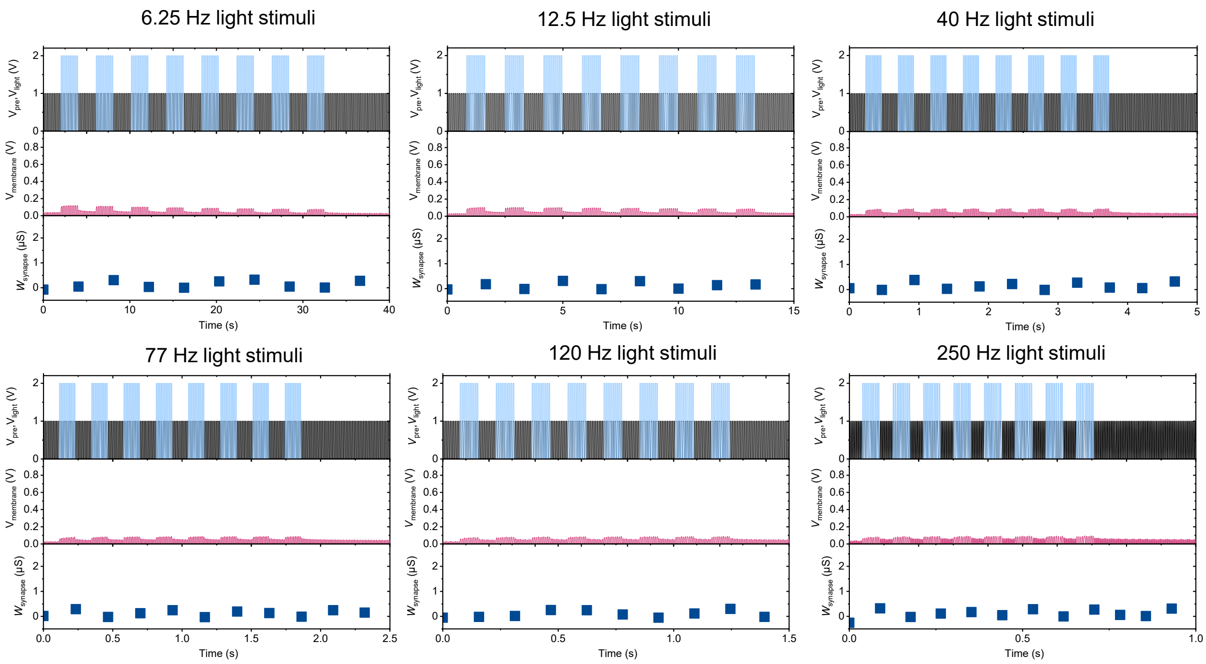

Fig. S35 | Real-time V_{mem} and W_{syn} response of BBL-based CMAN upon light stimuli (455 nm, 100 mW/cm^2) at a Ca^{2+} concentration of 10^{-4} M.

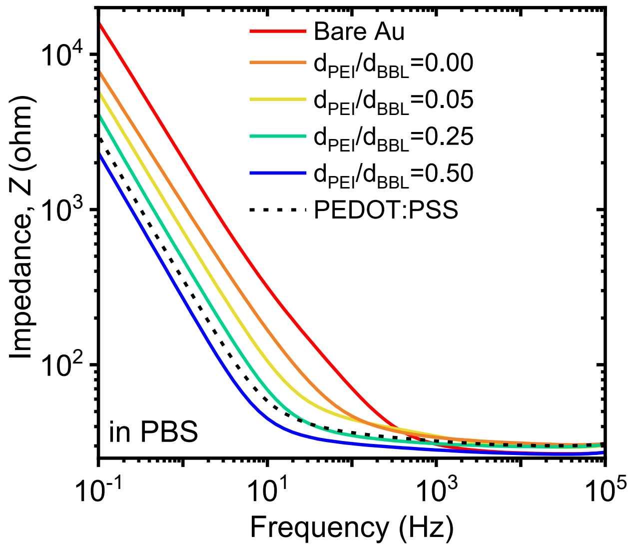

Fig. S36 | GIBS enables flexible neural interface with low impedance. All the materials are deposited on the PDMS/Cr/Au flexible substrate.

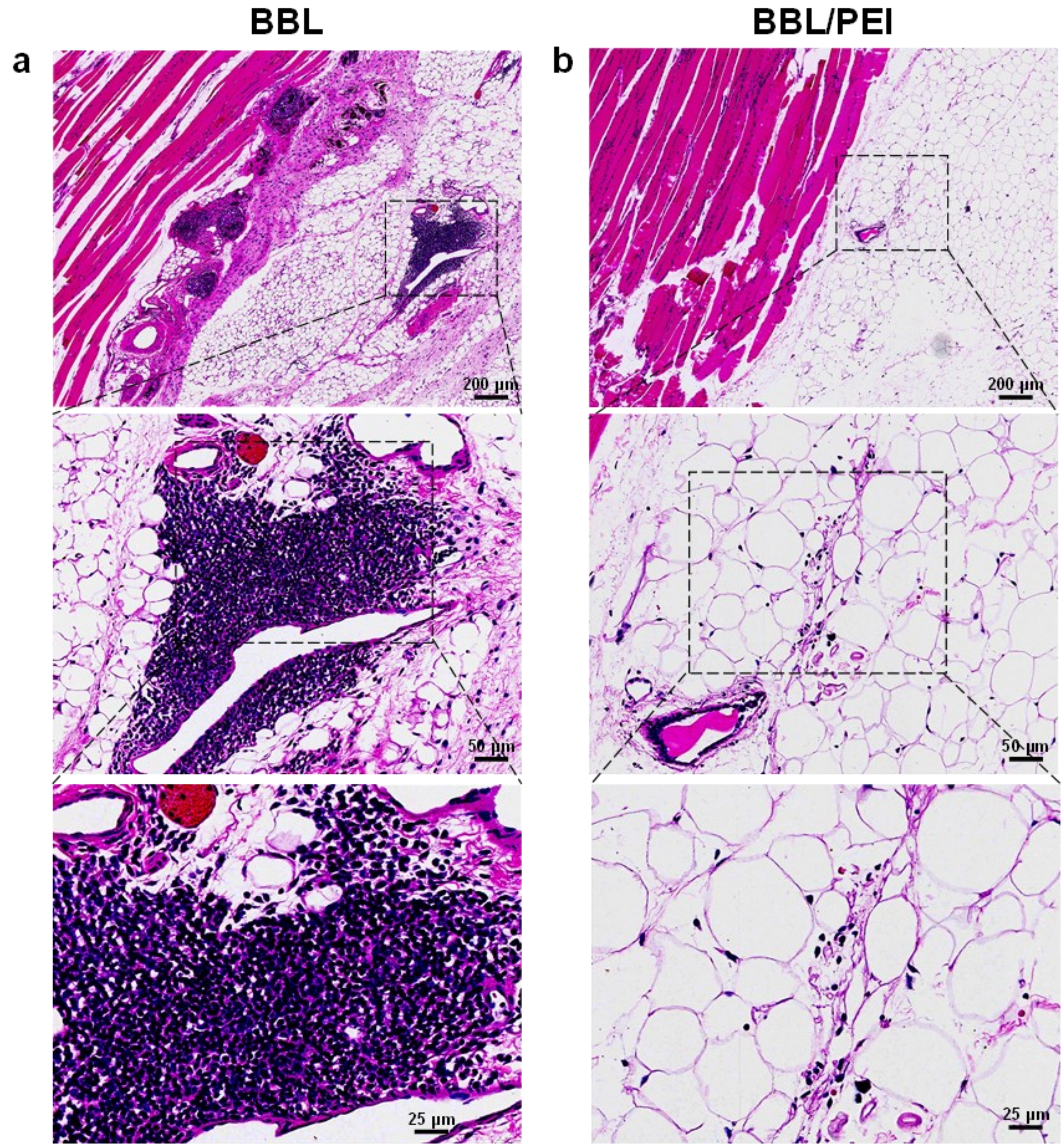

Fig. S37 | Hematoxylin-Eosin (H&E) staining images. a-b, H&E staining images of a, BBL and b, BBL/PEI soft electrode interfaced mouse leg tissue slice after 10 days of implantation**.** For BBL-interfaced tissue, much more neutrophils that feature spherical shape and dark violet color can be observed, indicating the inflammatory response of the tissue. In contrast, only a small number of neutrophils was observed on BBL/PEI interfaced tissue, indicating that GIBS can significantly improve the biocompatibility. This experiment was successfully repeated for one time per condition.

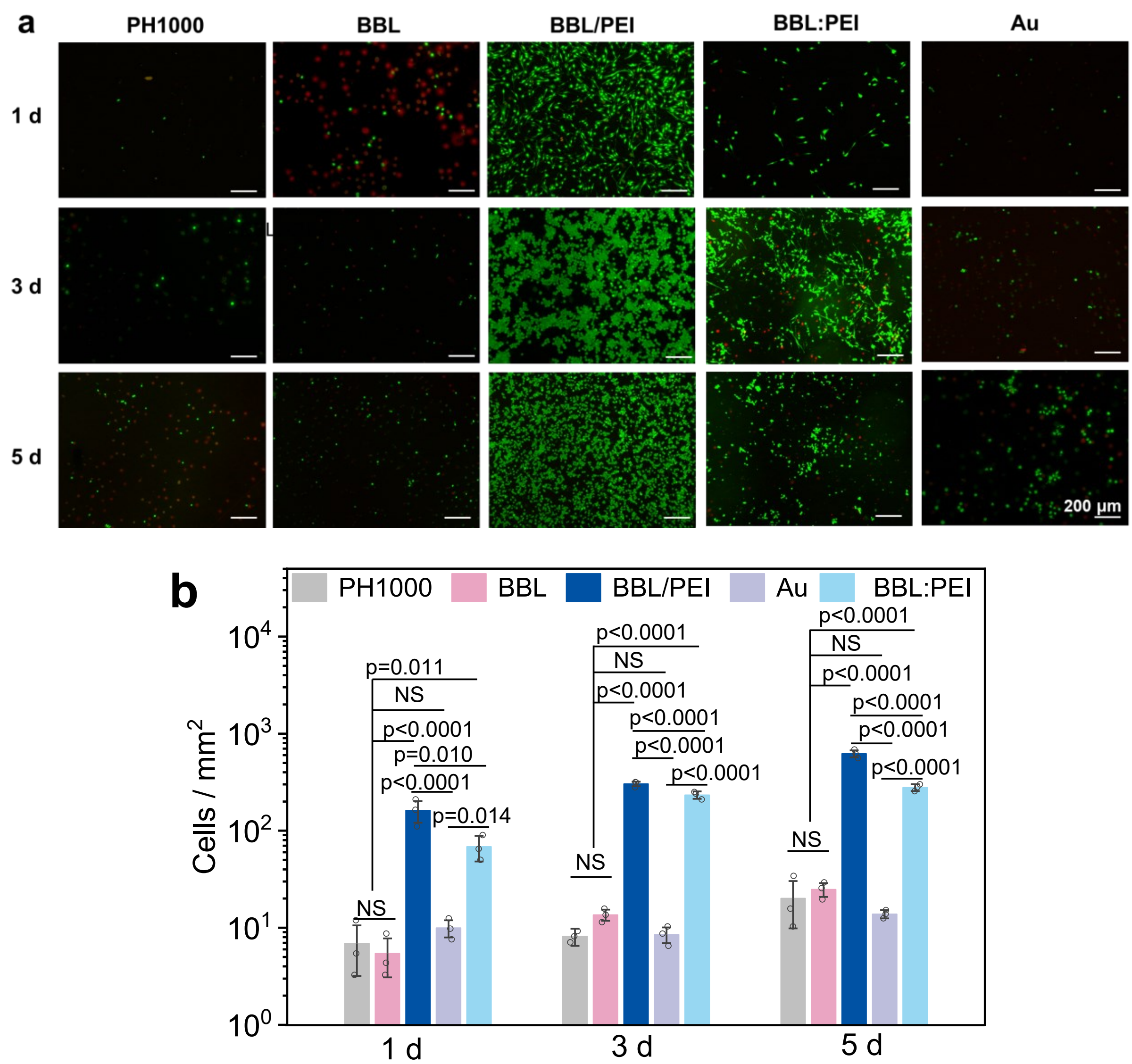

Fig. S38 | Fluorescence microscope results of the cells cultured on different cell-device interfaces. a, Live (in green)/dead (in red) staining images. b, quantified live cell numbers and c, MTT tested mitochondrial activities of PC-12 cells cultured on different device-cell interfaces. The statistical significance is analysed using one-way analyses of variance (ANOVA) and then a least-significant-difference (LSD) post hoc test is used to determine the level values of p, NS: no significance, error bars denote the s.d. for n = 3 independent samples, mean ± s.d. All the materials are deposited on the PDMS/Cr/Au flexible substrate.

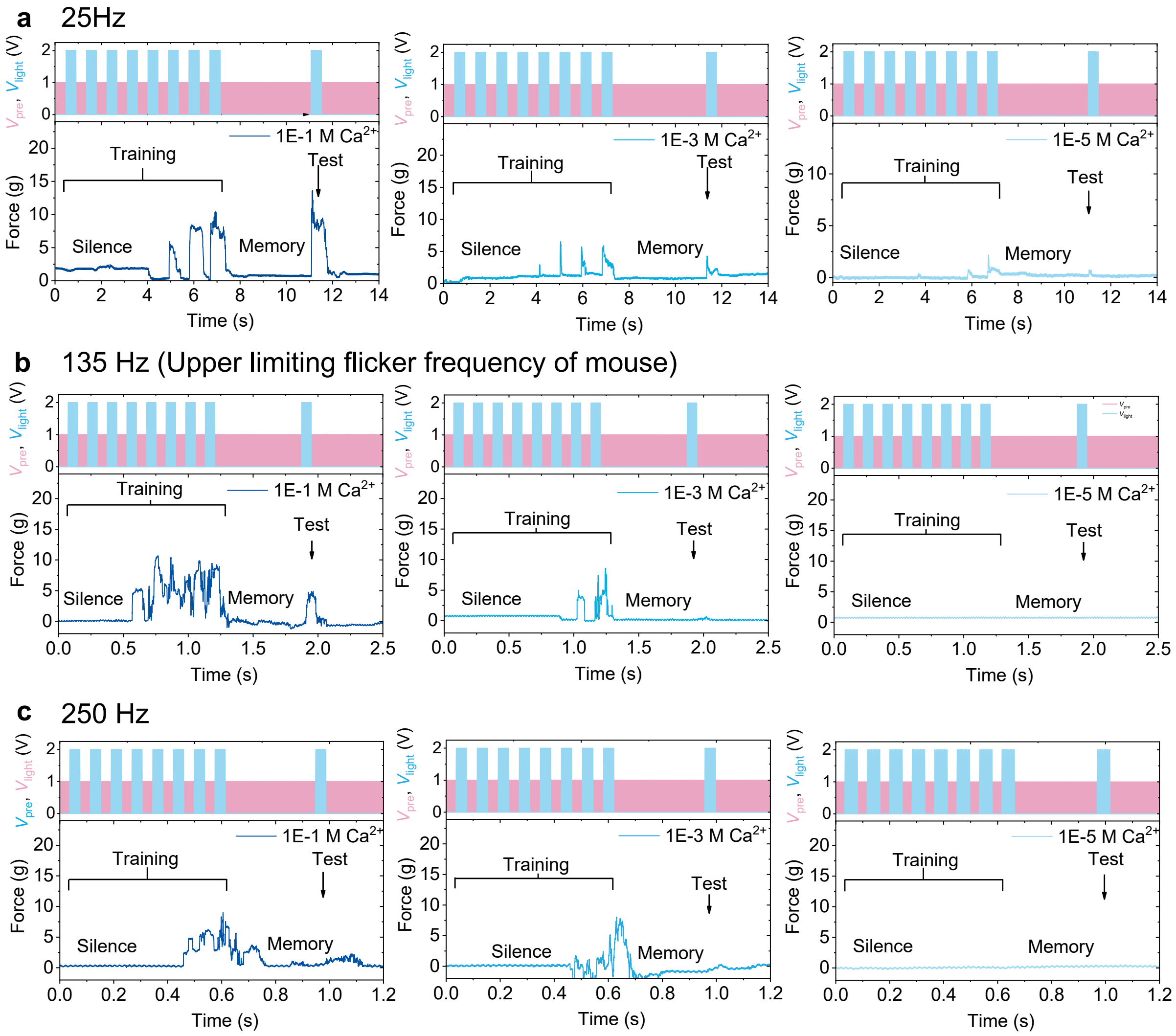

Fig. S39 | Conditioned reflex behavior of a CMAN implanted mouse. a-c, Real-time force of a hind leg depending on the frequency (25 Hz, 135 Hz and 250 Hz) of the light stimuli and surrounding chemical environment (10^{-1} M, 10^{-3} M and 10^{-5} M Ca^{2+}). Silence, training and memory represent the stage before, during and after stimuli, respectively.

References

1 Kim, Y. *et al.* A bioinspired flexible organic artificial afferent nerve. *Science* **360**, 998-1003 (2018).

2 Lee, Y. *et al.* A low-power stretchable neuromorphic nerve with proprioceptive feedback. *Nature Biomedical Engineering* **7**, 511-519 (2022).

3 Matrone, G. M. *et al.* A modular organic neuromorphic spiking circuit for retina-inspired sensory coding and neurotransmitter-mediated neural pathways. *Nature Communications* **15** (2024).

4 Wang, T. *et al.* A chemically mediated artificial neuron. *Nature Electronics* **5**, 586-595 (2022).

5 Cea, C. *et al.* Integrated internal ion-gated organic electrochemical transistors for stand-alone conformable bioelectronics. *Nature Materials* **22**, 1227-1235 (2023).

6 Cea, C. *et al.* Enhancement-mode ion-based transistor as a comprehensive interface and real-time processing unit for in vivo electrophysiology. *Nature Materials* **19**, 679-686 (2020).

7 Huang, W. *et al.* Vertical organic electrochemical transistors for complementary circuits. *Nature* **613**, 496-502 (2023).

8 Kim, J. *et al.* Monolithically integrated high-density vertical organic electrochemical transistor arrays and complementary circuits. *Nature Electronics* **7**, 234-243 (2024).

9 Zare Bidoky, F. *et al.* Sub‐3 V ZnO Electrolyte‐Gated Transistors and Circuits with Screen‐Printed and Photo‐Crosslinked Ion Gel Gate Dielectrics: New Routes to Improved Performance. *Advanced Functional Materials* **30** (2019).

10 Gao, G. *et al.* Triboiontronic Transistor of MoS2. *Advanced Materials* **31** (2018).

11 Cunha, I. *et al.* Reusable Cellulose‐Based Hydrogel Sticker Film Applied as Gate Dielectric in Paper Electrolyte‐Gated Transistors. *Advanced Functional Materials* **27** (2017).

12 Hess, L. H. *et al.* High-transconductance graphene solution-gated field effect transistors. *Applied Physics Letters* **99** (2011).

13 Sun, H. *et al.* Complementary Logic Circuits Based on High‐Performance n‐Type Organic Electrochemical Transistors. *Advanced Materials* **30** (2018).

14 Yang, C.-Y. *et al.* A high-conductivity n-type polymeric ink for printed electronics. *Nature Communications* **12** (2021).

15 Zhang, S. *et al.* Synergistic Effect of Multi‐Walled Carbon Nanotubes and Ladder‐Type Conjugated Polymers on the Performance of N‐Type Organic Electrochemical Transistors. *Advanced Functional Materials* **32** (2021).

16 Giovannitti, A. *et al.* N-type organic electrochemical transistors with stability in water. *Nature Communications* **7** (2016).

17 Surgailis, J. *et al.* Mixed Conduction in an N‐Type Organic Semiconductor in the Absence of Hydrophilic Side‐Chains. *Advanced Functional Materials* **31** (2021).

18 Paterson, A. F. *et al.* Water stable molecular n-doping produces organic electrochemical transistors with high transconductance and record stability. *Nature Communications* **11** (2020).

19 Chen, X. *et al.* n‐Type Rigid Semiconducting Polymers Bearing Oligo(Ethylene Glycol) Side Chains for High‐Performance Organic Electrochemical Transistors. *Angewandte Chemie International Edition* **60**, 9368-9373 (2021).

20 Feng, K. *et al.* Fused Bithiophene Imide Dimer‐Based n‐Type Polymers for High‐Performance Organic Electrochemical Transistors. *Angewandte Chemie International Edition* **60**, 24198-24205 (2021).
21 Feng, K. *et al.* Cyano-Functionalized n-Type Polymer with High Electron Mobility for High-Performance Organic Electrochemical Transistors. *Advanced Materials* **34**, 2201340 (2022).
22 Wu, W. *et al.* Selenophene Substitution Enabled High‐Performance n‐Type Polymeric Mixed Ionic‐Electronic Conductors for Organic Electrochemical Transistors and Glucose Sensors. *Advanced Materials* **36** (2023).
23 Wu, H. Y. *et al.* Influence of Molecular Weight on the Organic Electrochemical Transistor Performance of Ladder‐Type Conjugated Polymers. *Advanced Materials* **34** (2021).
24 Tang, H. *et al.* A solution-processed n-type conducting polymer with ultrahigh conductivity. *Nature* **611**, 271-277 (2022).
25 Li, P., Shi, J., Lei, Y., Huang, Z. & Lei, T. Switching p-type to high-performance n-type organic electrochemical transistors via doped state engineering. *Nature Communications* **13** (2022).
26 Wang, Y. *et al.* Acceptor Functionalization via Green Chemistry Enables High-Performance n-Type Organic Electrochemical Transistors for Biosensing, Memory Applications. *Advanced Functional Materials* **n/a**, 2304103 (2023).
27 Bischak, C. G., Flagg, L. Q., Yan, K., Li, C.-Z. & Ginger, D. S. Fullerene Active Layers for n-Type Organic Electrochemical Transistors. *ACS Applied Materials & Interfaces* **11**, 28138-28144 (2019).
28 Liu, K. K. *et al.* J‐Type Self‐Assembled Supramolecular Polymers for High‐Performance and Fast‐Response n‐Type Organic Electrochemical Transistors. *Advanced Functional Materials* **33** (2023).
29 Friedlein, J. T., McLeod, R. R. & Rivnay, J. Device physics of organic electrochemical transistors. *Organic Electronics* **63**, 398-414 (2018).
30 Xu, K. *et al.* Ground-state electron transfer in all-polymer donor–acceptor heterojunctions. *Nature Materials* **19**, 738-744 (2020).
31 Kraner, S. *et al.* Dielectric function of a poly(benzimidazobenzophenanthroline) ladder polymer. *Physical Review B* **91** (2015).
32 Pehlivan, İ. B., Marsal, R., Georén, P., Granqvist, C. G. & Niklasson, G. A. Ionic relaxation in polyethyleneimine-lithium bis(trifluoromethylsulfonyl) imide polymer electrolytes. *Journal of Applied Physics* **108**, 074102 (2010).